

The Circumstellar Environment of High Mass Protostellar Objects. III Evidence of Infall ?

G. A. Fuller¹, S. J. Williams¹ and T.K. Sridharan²

¹ Physics Department, UMIST, P.O. Box 88, Manchester M60 1QD, UK

e-mail: Gary.Fuller@manchester.ac.uk, Stewart.Williams@manchester.ac.uk

² Harvard-Smithsonian Center for Astrophysics, 60 Garden Street, MS 78, Cambridge, MA 02138, USA

e-mail: tksridha@cfa.harvard.edu

Received ; accepted

Abstract. The results are presented of a molecular line survey to search for the spectral signature of infall towards 77 850 μ m continuum sources believed to be candidate high mass protostellar objects. Up to six different transitions, HCO⁺ J= 1 \rightarrow 0, J= 3 \rightarrow 2 and J= 4 \rightarrow 3, H₂CO 2₁₂ - 1₁₁, N₂H⁺ J= 1 \rightarrow 0 and H¹³CO⁺ J= 3 \rightarrow 2, were observed towards each source. Towards the peak of the 850 μ m emission, N₂H⁺ was typically strong, with a peak antenna temperature of \sim 1.5K, with a typical linewidth of \sim 2 km s⁻¹. The good agreement between the velocity and velocity width of the N₂H⁺ and H¹³CO⁺ emission suggests that both species are tracing similar material in the sources. With respect to the velocity of the N₂H⁺, there is a statistically significant excess of blue asymmetric line profiles in both the HCO⁺ J= 1 \rightarrow 0 and H₂CO transitions. This excess reaches levels similar to that seen towards samples of low mass protostars, and suggests that the material around these high mass sources is infalling. We identify 22 promising candidate infall sources which show at least one blue asymmetric line profile and no red asymmetric profiles. The infall velocity is estimated to be in the range of 0.1 km s⁻¹ to 1 km s⁻¹ with an implied mass accretion rate of between $2 \times 10^{-4} M_{\odot}/\text{yr}$ and $10^{-3} M_{\odot}/\text{yr}$.

Key words. Stars: formation – ISM: molecules – ISM: kinematics and dynamics – HII regions

1. Introduction

The mass, energy and momentum input from high mass stars ($M_* > 8M_{\odot}$) shapes the physical and chemical properties of the interstellar medium in a galaxy and can control the ISM's evolution. Once formed, the high mass stars, although relatively few in number, rapidly determine a molecular cloud's future evolution, regulating the formation of lower mass stars. Despite their importance there is as yet no generally accepted view of how high mass stars form. Proposed models range from accretion driven formation (McKee & Tan, 2002, 2003), similar to that proposed for the formation of low mass stars, competitive accretion in clusters (Bonnell, Vine & Bate 2004) or even the agglomeration of lower mass protostars (Bonnell, Bate & Zinnecker 1998).

Recent work identifying candidate high mass protostellar objects (e.g Lumsden et al. 2002; Molinari et al. 1996; Sridharan et al. 2002) has provided samples of luminous young sources with which to address some of the uncertainties about high mass star formation. Identifying and studying the accretion flows which collect the material out of which stars form, either directly or indirectly, is an important aspect of understanding high-mass star formation. Evidence for the infall of material around a source can be provided by analysis of molecular line profiles. Any ordered motions such as rotation, outflow or infall can produce recognisable signatures in the line profiles and their spatial distribution (e.g. Adelson & Leung 1988). However unlike outflow or rotation which give rise to both red and blue asymmetric lines, infall produces only blue asymmetric lines. The profiles of optically thick lines from infalling material have stronger blue shifted emission than red shifted emission (Leung & Brown 1977; Anglada et al. 1987; Zhou 1992; Walker, Narayanan & Boss 1994), provided that the excitation temperature of the molecules increases towards the centre of the region. This asymmetry arises as the blue shifted emission from the approaching warm gas on the far side of the centre of contraction suffers less extinction than the emission from the receding, nearside, material. Although for any one object, outflow or rotation could also produce a blue asymmetric line profile along a particular line of sight to a source, for an ensemble of sources the presence of infall should manifest itself as an excess of blue asymmetric line profiles compared to red asymmetric profiles. On the other hand, an unbiased sample of sources dominated by outflows or rotation would be expected to produce roughly equal numbers of blue and red asymmetric lines.

An excess of blue asymmetric line profiles is now well established towards low-mass star forming regions, providing strong evidence for infall towards these regions. Not only has it been detected in a variety of different tracers and transitions towards low mass protostars but also towards starless cores (Mardones et al. 1997; Lee et al. 1999, 2001, 2004; Williams et al 1999; Park et al. 1999; Gregersen & Evans 2000; Gregersen et al. 2000; Di Francesco et al. 2001; Belloche et al. 2002). In this paper we present the first results of a survey for the infall line asymmetry towards a sample of candidate high mass protostellar objects (HMPOs).

Table 1. Source Positions. The source numbers are from Williams et al. (2004; WFS) but the tabulated positions are the observed positions, which as discussed in the text do not necessary precisely agree with those in WFS. The name of the corresponding IRAS point source is also given.

Source	IRAS	RA(2000)	Dec(2000)	Source	IRAS	RA(2000)	Dec(2000)
2	05358+3543	05:39:12.6	+35:45:50	62	18540+0220	18:56:36.7	+02:24:44
3	05490+2658	05:52:11.0	+27:00:32	64	18553+0414	18:57:53.3	+04:18:17
5	05490+2658	05:52:12.1	+26:59:35	65	18566+0408	18:59:10.0	+04:12:13
6	05553+1631	05:58:13.5	+16:31:59	66	19012+0536	19:03:45.1	+05:40:45
8	18089-1732	18:11:51.4	-17:31:35	67	19035+0641	19:06:01.3	+06:46:37
12	18090-1832	18:12:01.8	-18:32:01	68	19074+0752	19:09:53.4	+07:57:14
13	18102-1800	18:13:11.5	-18:00:03	70	19175+1357	19:19:48.4	+14:02:27
14	18151-1208	18:17:58.2	-12:07:26	71	19175+1357	19:19:48.8	+14:02:47
15	18159-1550	18:18:48.3	-15:48:58	72	19217+1651	19:23:58.7	+16:57:39
16	18182-1433	18:21:09.1	-14:31:49	73	19220+1432	19:24:19.7	+14:38:03
17	18223-1243	18:25:10.7	-12:42:28	74	19266+1745	19:28:55.5	+17:52:00
18	18247-1147	18:27:31.5	-11:45:56	75	19282+1814	19:30:23.1	+18:20:25
19	18264-1152	18:29:14.4	-11:50:24	77	19403+2258	19:42:27.2	+23:05:12
20	18272-1217	18:30:02.3	-12:15:38	79	19410+2336	19:43:11.0	+23:44:06
21	18272-1217	18:30:02.7	-12:15:13	80	19411+2306	19:43:18.1	+23:13:59
22	18290-0924	18:31:43.3	-09:22:28	82	19413+2332	19:43:29.0	+23:40:22
23	18290-0924	18:31:44.1	-09:22:16	83	19471+2641	19:49:09.9	+26:48:52
25	18306-0835	18:33:23.3	-08:33:30	85	20051+3435	20:07:04.5	+34:44:44
27	18308-0841	18:33:33.0	-08:39:10	87	20081+2720	20:10:13.1	+27:28:17
28	18310-0825	18:33:47.9	-08:23:50	88	20081+2720	20:10:15.9	+27:28:10
29	18337-0743	18:36:27.9	-07:40:25	90	20126+4104	20:14:25.8	+41:13:33
30	18345-0641	18:37:16.8	-06:38:32	91	20205+3948	20:22:20.1	+39:58:20
33	18348-0616	18:37:30.3	-06:14:11	93	20216+4107	20:23:23.7	+41:17:43
34	18372-0541	18:39:55.9	-05:38:52	94	20293+3952	20:31:12.6	+40:03:18
35	18385-0512	18:41:12.8	-05:08:59	95	20319+3958	20:33:49.1	+40:08:35
36	18426-0204	18:45:12.2	-02:01:12	96	20332+4124	20:34:58.8	+41:34:47
37	18431-0312	18:45:45.6	-03:09:22	97	20332+4124	20:35:00.9	+41:35:02
38	18437-0216	18:46:21.6	-02:12:22	99	20343+4129	20:36:06.4	+41:39:57
39	18437-0216	18:46:22.4	-02:14:20	100	20343+4129	20:36:08.0	+41:39:57
42	18440-0148	18:46:36.4	-01:45:22	101	22134+5834	22:15:09.6	+58:49:06
43	18445-0222	18:47:10.8	-02:19:06	103	22551+6221	22:57:06.8	+62:37:25
44	18447-0229	18:47:21.6	-02:26:11	106	22570+5912	22:58:58.9	+59:27:42
48	18449-0158	18:47:35.6	-01:55:26	107	22570+5912	22:59:04.8	+59:28:19
50	18454-0136	18:48:02.1	-01:33:28	108	23033+5951	23:05:24.7	+60:08:13
51	18460-0307	18:48:39.7	-03:03:56	109	23139+5939	23:16:10.1	+59:55:29
54	18470-0044	18:49:36.7	-00:41:05	110	23151+5912	23:17:20.8	+59:28:49
55	18472-0022	18:49:52.2	-00:18:57	111	23545+6508	23:57:02.4	+65:24:37
57	18488+0000	18:51:24.8	+00:04:19	112	23545+6508	23:57:06.0	+65:24:48
59	18521+0134	18:54:40.6	+01:38:04				

The sources observed were originally selected from the IRAS point source catalogue by Sridharan et al. (2002) based on criteria established by Ramesh & Sridharan (1997). The IRAS sources were selected to be bright with fluxes of greater than 90Jy and 500 Jy at 60 μ m and 100 μ m respectively and to have colours in the IRAS bands which match the Wood & Churchwell (1989) criteria for UCHII regions but not to have the radio continuum emission expected from a UCHII region. These characteristics were chosen to identify sources which are luminous and have dust shells similar to UCHII regions but have not formed an HII region and so may represent earlier stages in the evolution of mass young stars. These sources have subsequently been studied by Beuther et al. (2002b,a) and Williams, Fuller & Sridharan (2004, 2005).

Table 2. Observed transitions and telescope parameters. η is the telescope beam efficiency, FWHM the full width half maximum beam width and Δv the channel spacing of the correlator. The references for the line frequencies are 1 - Caselli et al. (1995), 2 - Lovas (1992, 2003), 3 - online version of Pickett et al. (1998), 4 - Gregersen & Evans (2001)

Species	Transition	Frequency (GHz)	Reference	Telescope	η	FWHM (")	Δv (km/s)
N ₂ H ⁺	J=1-0	93.1737767±0.000007	1	IRAM 30m	0.78	26"	0.13
HCO ⁺	J=1-0	89.188518±0.000009	2	IRAM 30m	0.78	29"	0.13
HCO ⁺	J=3-2	267.557625	3	IRAM 30m	0.69	20"	0.04
HCO ⁺	J=4-3	356.734288	3	JCMT	0.63	14"	0.26
H ¹³ CO ⁺	J=3-2	260.255339 ± 0.0000035	4	JCMT	0.69	20"	0.09
H ₂ CO	J _{kk'} = 2 ₁₂ - 1 ₁₁	140.839518±0.000007	2	IRAM 30m	0.69	17"	0.08

Table 3. RMS T_A^* noise levels in spectra.

Source	HCO ⁺			H ₂ CO	Source	HCO ⁺			H ₂ CO	Source	HCO ⁺			H ₂ CO
	1-0 (K)	3-2 (K)	4-3 (K)			1-0 (K)	3-2 (K)	4-3 (K)			1-0 (K)	3-2 (K)	4-3 (K)	
2	0.07	...	0.10	...	36	0.11	...	0.04	0.08	77	0.06	...	0.08	0.07
3	0.06	...	0.13	...	37	0.10	...	0.05	0.07	79	0.03	...	0.09	0.07
5	0.06	39	0.04	...	0.04	0.09	80	0.06	...	0.59	0.08
6	0.07	...	0.10	...	38	0.07	0.32	0.03	0.10	82	0.04	...	0.08	0.08
8	0.10	0.42	0.11	0.08	42	0.07	...	0.03	0.08	83	0.06	...	0.09	0.05
12	0.07	0.42	0.07	0.09	43	0.07	0.20	0.08	0.06	85	0.05	...	0.16	0.07
13	0.04	...	0.09	0.07	44	0.08	...	0.05	0.08	88	0.05	...	0.14	0.07
14	0.02	...	0.08	0.06	48	0.08	0.27	0.07	0.08	87	0.05	...	0.08	0.08
15	0.06	...	0.07	0.06	50	0.06	0.23	0.05	0.05	90	0.06	...	0.11	0.04
16	0.04	...	0.07	0.06	51	0.08	...	0.05	0.07	91	0.05	...	0.11	0.07
17	0.04	...	0.12	0.06	54	0.07	0.26	0.08	0.07	93	0.04	0.23	0.09	0.06
18	0.18	...	0.18	0.06	55	0.08	...	0.06	0.07	94	0.06	...	0.09	0.07
19	0.06	...	0.11	0.06	59	0.09	0.28	0.05	0.07	95	0.05	0.23	0.06	0.06
21	0.09	...	0.17	0.06	62	0.06	0.29	0.04	0.07	96	0.07	0.23	0.07	0.07
20	0.05	0.39	0.13	0.09	64	0.03	0.19	0.05	0.05	97	0.07	0.20	0.08	0.06
23	0.09	...	0.09	0.07	65	0.07	0.23	0.26	0.05	99	0.05	0.21	0.15	0.07
22	0.07	0.34	0.08	0.09	66	0.04	0.24	0.07	0.07	100	0.05	0.20	0.09	0.07
25	0.10	...	0.17	0.08	67	0.05	0.24	0.09	0.07	101	0.09	0.28	0.10	0.07
27	0.09	...	0.12	0.08	68	0.06	0.23	0.05	0.06	106	0.07	0.32	0.07	0.07
28	0.09	...	0.09	0.07	71	0.08	...	0.10	0.07	107	0.06	0.25	0.08	0.06
29	0.09	...	0.10	0.08	70	0.07	0.24	0.08	0.06	108	0.07	0.25	0.06	0.06
30	0.09	...	0.07	0.08	72	0.05	...	0.10	0.08	109	0.07	0.16	0.07	0.05
33	0.08	...	0.38	0.08	73	0.07	0.24	0.11	0.07	110	0.05	0.31	0.05	0.07
34	0.09	...	0.04	0.07	74	0.07	0.08	111	0.07	0.16	0.08	0.04
35	0.10	...	0.08	0.07	75	0.06	...	0.09	0.08	112	0.07	0.25	0.22	0.07

2. Observations

To search for evidence of infall, single point observations were made towards the peaks of the 850 μ m SCUBA sources identified by Williams, Fuller & Sridharan (2004, hereafter WFS) as associated with the IRAS sources selected by Sridharan et al. (2002). The observed positions are listed in Table 1. Since the target positions were derived from an initial reduction of the SCUBA images, the positions do not necessarily precisely agree with more accurate positions published in WFS but typically agree within a few arcseconds. There are, however, six sources where the positions are discrepant by 14" or more (WFS43, 48, 54, 57, 77, 83).

The observations were carried out using the 30m telescope of the Institut de Radioastronomie Millimétrique (IRAM)¹ near Granada, Spain and the 15m James Clerk Maxwell Telescope (JCMT) on Mauna Kea, Hawaii². The frequencies of the lines observed, together with other frequency dependent parameters are listed in Table 2. The uncertainties in the line frequencies (where known) introduce a maximum uncertainty of ± 0.03 km s⁻¹ (for the HCO⁺ 1-0) to the derived line velocity.

¹ IRAM is supported by INSU/CNRS (France), MPG (Germany) and IGN (Spain)

² The JCMT is operated by the Joint Astronomy Centre in Hilo, Hawaii on behalf of the parent organizations Particle Physics and Astronomy Research Council in the United Kingdom, the National Research Council of Canada and The Netherlands Organization for Scientific Research.

At the JCMT the $J=4 \rightarrow 3$ transition of HCO^+ and the $J=3 \rightarrow 2$ transition of H^{13}CO^+ were observed using the RxB3 and RxA3 receivers respectively over the periods from April to June 2001 and May to June 2002. The HCO^+ observations used both polarization channels of RxB3 and after checking that the two channels agreed in line intensity and center velocity the two channels were averaged together for analysis. A portion of these observations were made using in-band frequency switching. This resulted in curved, but smooth baselines which were removed using polynomial fits. The H^{13}CO^+ observations were position switched using the single channel of RxA3. The off positions were typically $14'$ away from the sources at a position $(+10', +10')$ from the source. The typical rms noise level reached during the observations was 0.08K for the HCO^+ and 0.1K for the H^{13}CO^+ and the typical system temperatures were around 750K and 390K respectively. All the JCMT observations made use of the DAS autocorrelator spectrometer. The channel separation used for each of the transitions is listed in Table 2. The JCMT data were all initially reduced using the JCMT SPECX package and then imported to the IRAM spectral line reduction package CLASS for comparison with the IRAM observations.

The IRAM observations were carried out between December 2001 and January 2002 and in August 2002. The N_2H^+ and HCO^+ $J=1 \rightarrow 0$ transitions were simultaneously observed in different polarizations using the two 3mm receivers. The typical system temperatures and rms noise levels in the resulting spectra were 120K and 0.07K , and 130K and 0.07K for the HCO^+ and N_2H^+ respectively. The H_2CO line was then observed separately using both the facility 2mm receivers. The two H_2CO spectra were checked for consistency before being averaged together for analysis resulting in spectra with typical system temperatures and noise levels of $\sim 190\text{K}$ and $\sim 0.07\text{K}$ respectively. During the August 2002 observations the $J=3 \rightarrow 2$ transitions of HCO^+ and H^{13}CO^+ were observed, one with each of the 1mm receiver systems, simultaneously with H_2CO . In no case did the observations of H^{13}CO^+ provide a higher signal to noise detection than the JCMT observations and only the JCMT data on this transition are presented here and considered in the analysis. The rms noise levels for each of the HCO^+ and H_2CO spectra are given in Table 3. All the IRAM observations were made using position switching with the same off positions as used at the JCMT. The sources were observed using the autocorrelator spectrometer and during the August 2002 run, the newer VESPA correlator. The IRAM data were reduced using the CLASS package.

Considering both the JCMT and IRAM data, there was only evidence of off-position emission contaminating the observations in about four spectra in total and in all cases the emission at the off position was considerably weaker than towards the source, easily identifiable and did not affect the determination of the line peak velocity. The pointing and focus were regularly checked during the observations with both telescopes. The largest pointing errors seen were $\sim 3''$ and typically the pointing offsets were less than $2''$.

Spectra towards the sources are shown in Figure 1 and 2. The hyperfine structure of the N_2H^+ transition produces three components in the spectra. None of the other transitions have hyperfine structure.

2.1. Reduction

The reduction and analysis of the line profiles to look for evidence of infall asymmetry is primarily concerned with the line velocities and widths, and we will limit the discussion to just these aspects of the emission. The line intensities and column densities which can be inferred from the optically thin N_2H^+ and H^{13}CO^+ emission can provide useful information on the circumstellar material, but we will delay the discussion of these aspects of the emission until a later work.

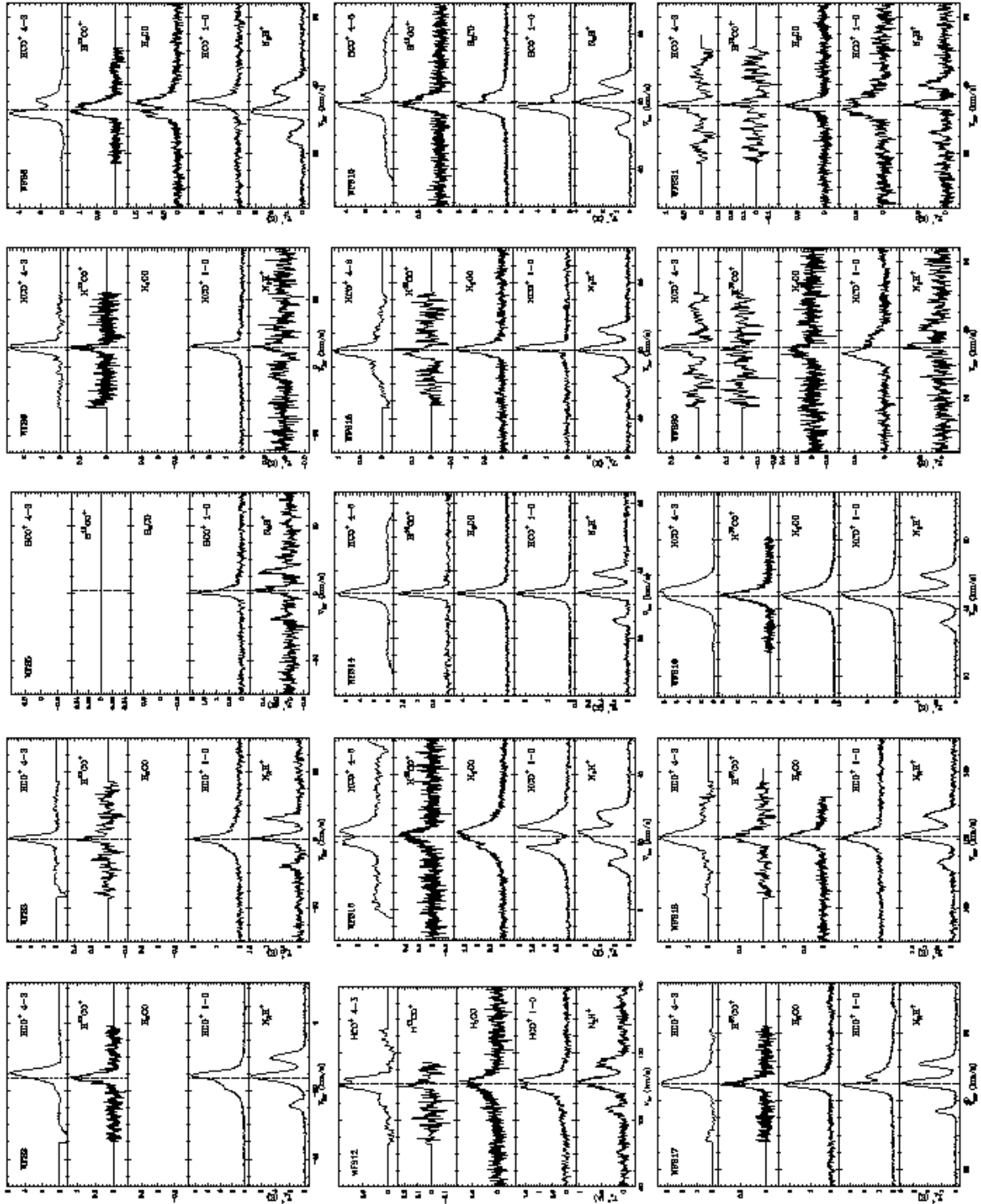


Fig. 1. Spectra of sources. For each the source, from bottom to top, the figure shows the spectrum of N_2H^+ , $HCO^+ J=1 \rightarrow 0$, H_2CO , $H^{13}CO^+ J=3 \rightarrow 2$ and $HCO^+ J=4 \rightarrow 3$. The dashed vertical line shows the best fit velocity for the N_2H^+ . For presentation some of the $H^{13}CO^+$ spectra have been rebinned to 0.27 km/s channels. The intensity scale is $T_A^* \text{ for all the spectra}$.

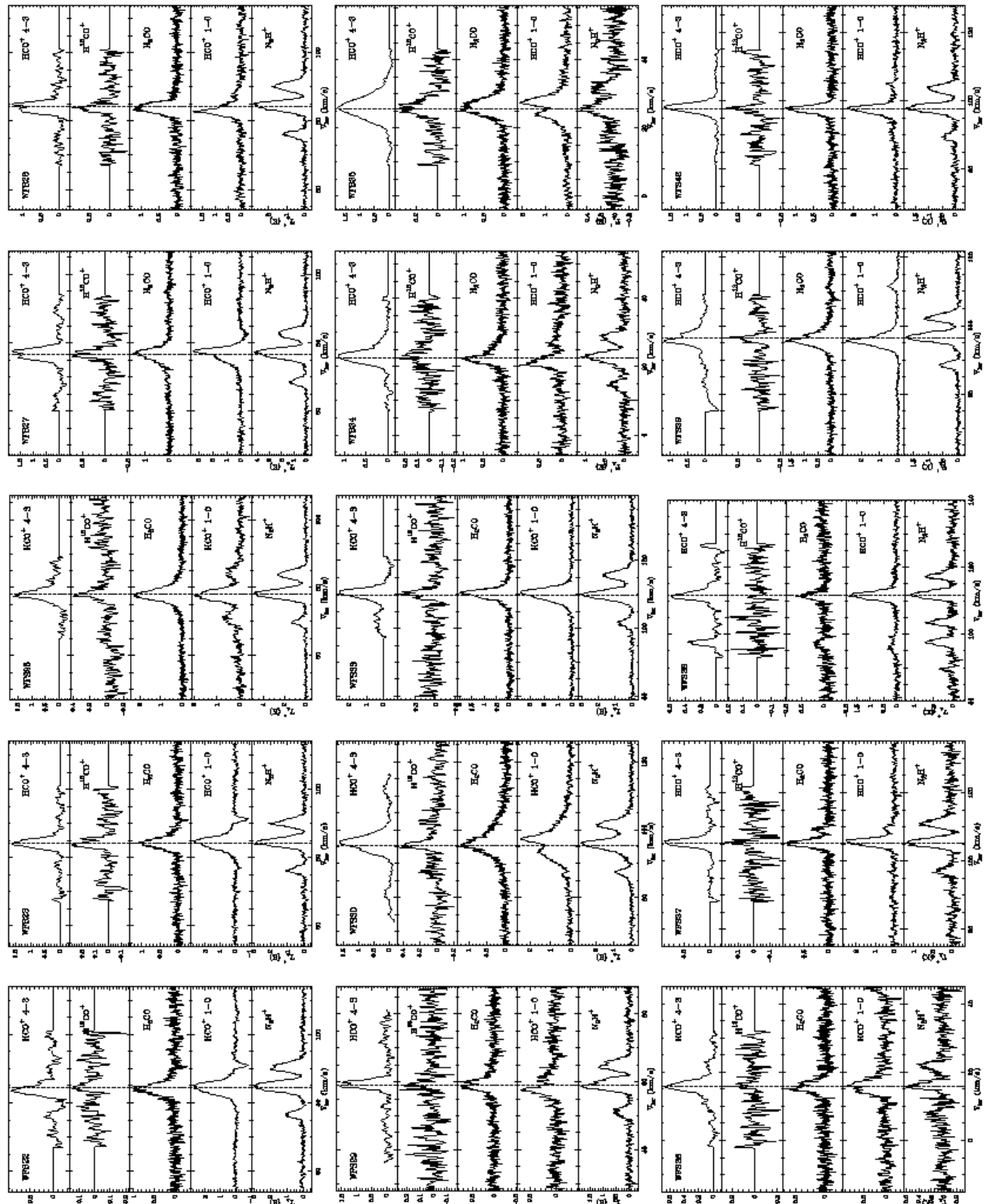


Figure 1 continued.

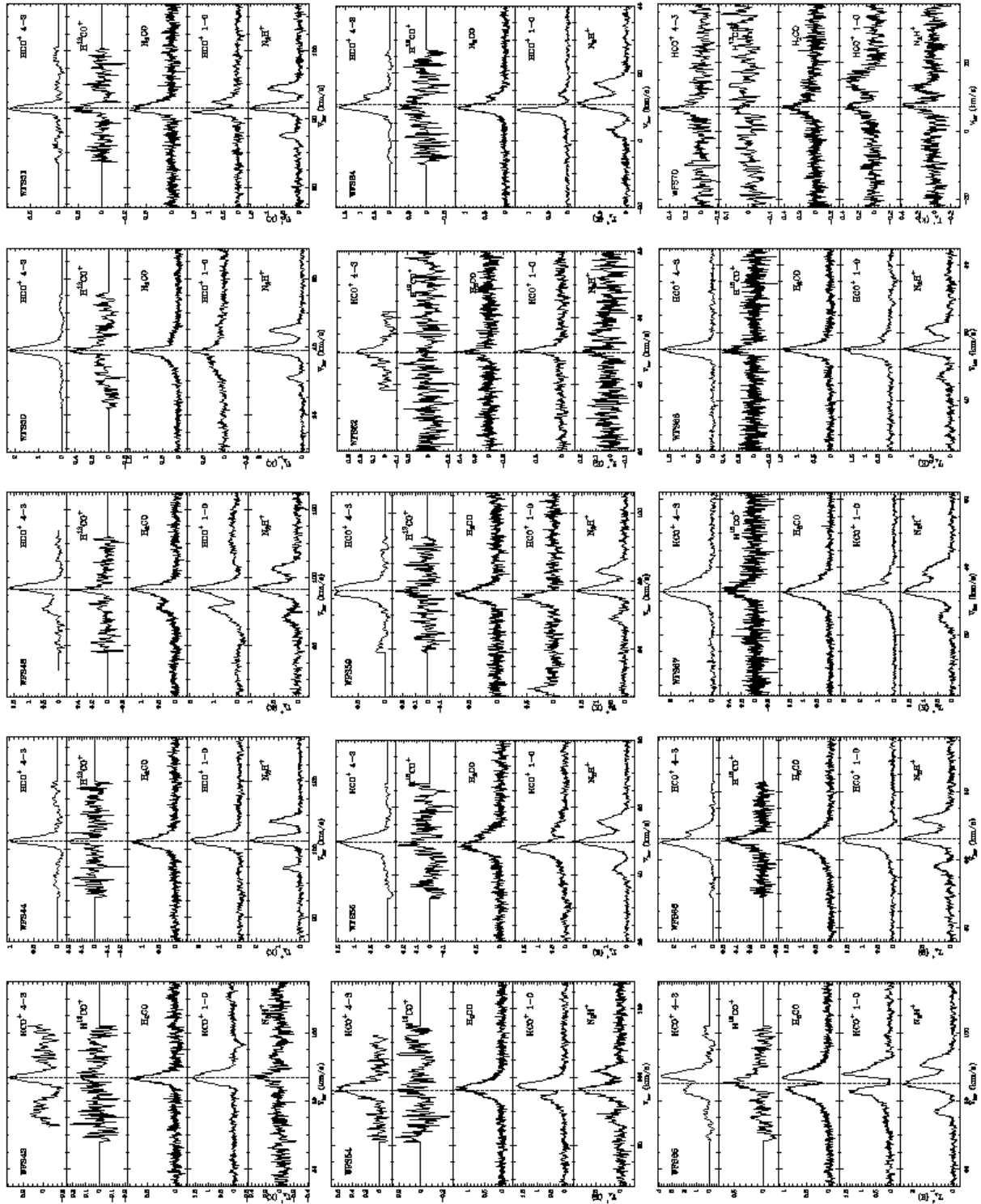


Figure 1 continued.

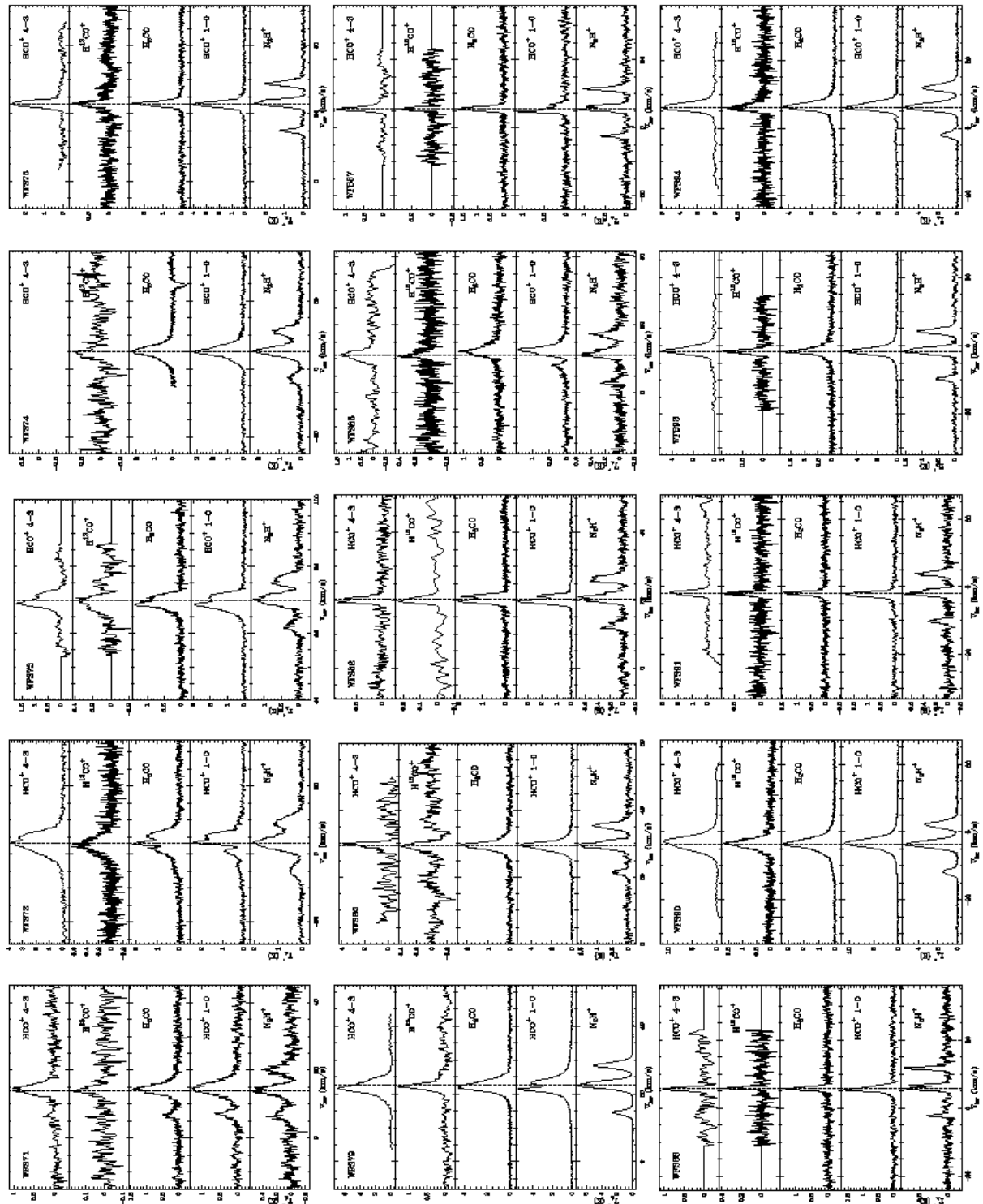


Figure 1 continued.

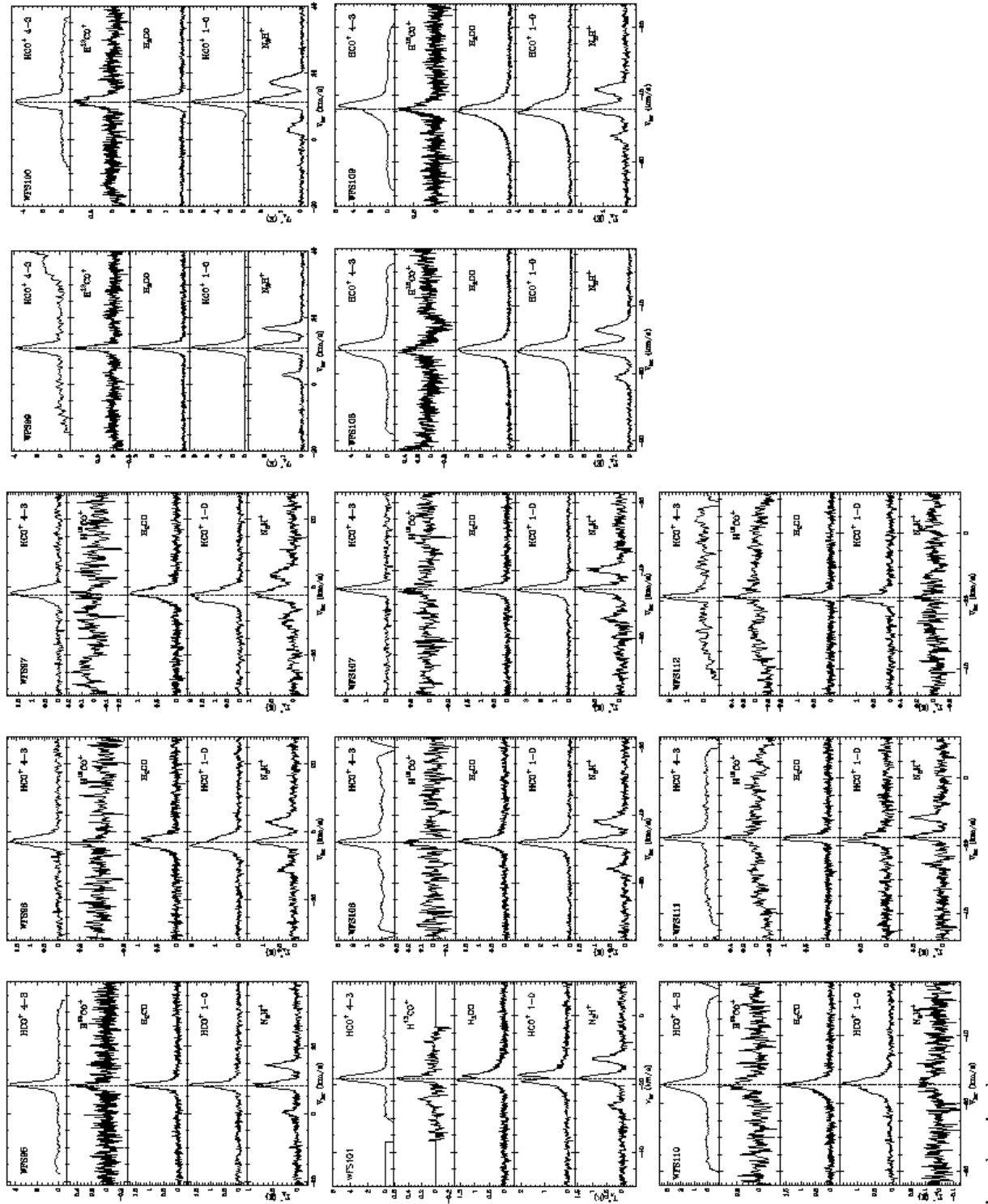


Figure 1 continued.

The N_2H^+ spectra were fitted with the seven hyperfine components given in Table 4 using the hyperfine fitting routines in CLASS to determine the properties of the emission. The parameters defining the hyperfine components are listed in Table 4 and the results for the fit for each source are given in Table 5. The majority of the spectra are well fitted by a single gaussian velocity component, however for some sources, for example WFS2, a single component is not a good model. In Table 5 these sources can be identified as the sources for which the residual in the region where the line was fitted is significantly larger than in a region of the spectrum free from emission. Most of the spectra are also consistent with optically thin emission, although again there are exceptions, for example WFS 13 and WFS 38.

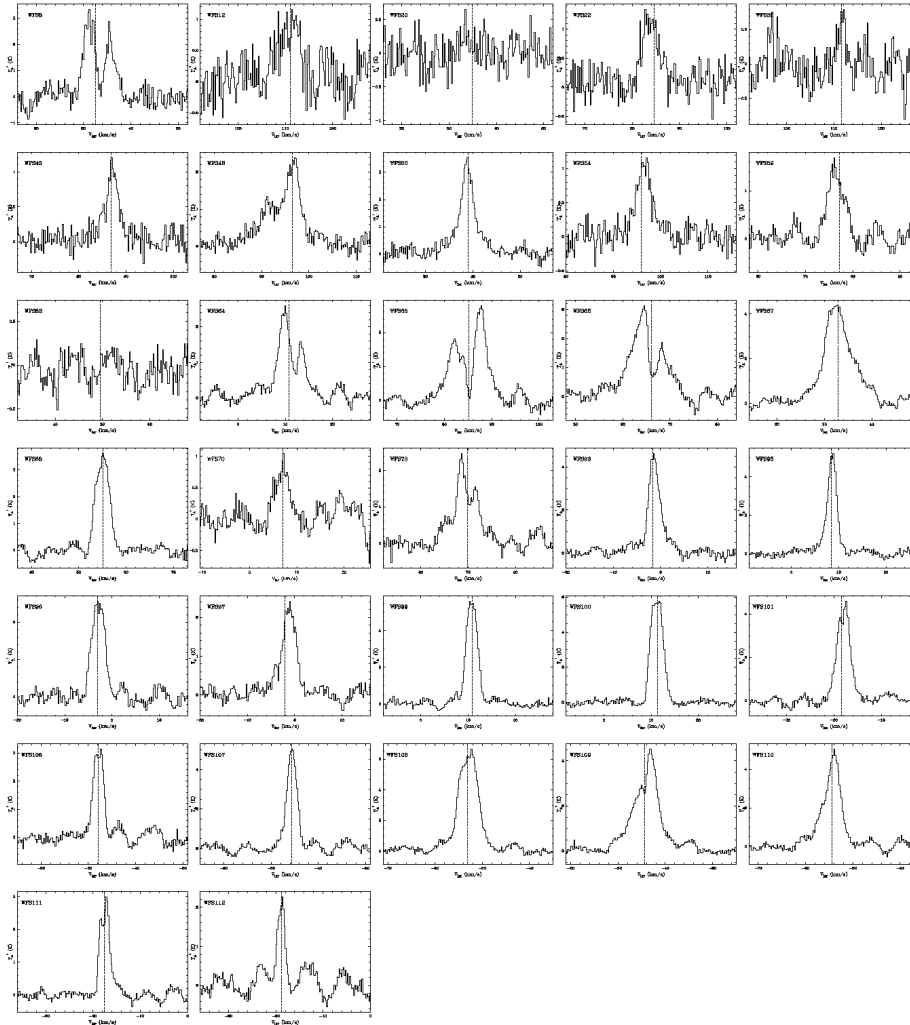


Fig. 2. Spectra of $\text{HCO}^+ J=3 \rightarrow 2$ towards the sources. The data is from the IRAM 30m telescope. The dashed vertical lines shows the N_2H^+ best fit velocity for each source. For presentation the spectra have been rebinned to 0.22 km/s channels. The intensity axis is in units of T_A^* in Kelvin.

Table 4. Hyperfine structure of N_2H^+ . The velocity offset is measured with respect to the $F_1F \rightarrow F'_1F'$ = 23 \rightarrow 12 component for which we adopt a frequency of 93.1737767 GHz. The statistical weight of the hyperfine component is given in the column labelled Weight.

Component $F_1F \rightarrow F'_1F'$	Velocity offset (km/s)	Weight
10 \rightarrow 11	6.94	0.04
12 \rightarrow 12	5.98	0.18
11 \rightarrow 10	5.54	0.11
22 \rightarrow 11	0.96	0.18
23 \rightarrow 12	0.00	0.26
21 \rightarrow 11	-0.61	0.11
01 \rightarrow 12	-8.01	0.11

The only sources towards which N_2H^+ was not detected are WFS 57, WFS 83, and WFS 103. Towards WFS77 the N_2H^+ line was very weak and only very poorly detected. No H^{13}CO^+ emission was detected towards these sources and these sources are not considered any further in the analysis below. The N_2H^+ line is also very weak towards WFS 110 and WFS 112 and these sources are also excluded from the analysis below. The source WFS 48, whilst observed here and by Williams et al. (2004), is not part of the Sridharan et al. (2002) sample and is not included in any of the analysis discussed below. For consistency in probing the material along the line of sight to the central sources in each object, the two remaining objects which were observed at (relatively) large offsets from the submillimetre peak (WFS43 and 54; Sec 2) were also excluded from the analysis below.

The results of fitting single Gaussian components to the H^{13}CO^+ lines for which the line peak intensity is greater than 2.5 times the rms noise are given in Table 6. Comparing the rms of the residuals of the line fit with the rms noise in an emission free region of the spectrum shows that all these spectra are well modelled by these single Gaussian components. The 2.5 times the rms noise limit corresponds to a detection in the integrated intensity of more than 10 for a line with a typical width of 2 km s^{-1} .

The other transitions show a range of line shapes ranging from Gaussian profiles to profiles with multiple peaks and line wings. To measure the line peak velocity of these lines, a parabolic fit over a number of channels around the line centre, covering the velocity range out to where the line reached about half of its peak intensity, was used. This method was preferred to using Gaussian fits to avoid any line wings influencing the fitted velocities. These parabolic fits were all inspected to confirm that they provided a good measure of the velocity of the line peak. The results of these parabolic fits are shown in Table 7. As discussed below (§ 4), since the HCO^+ $J = 4 \rightarrow 3$ transition shows the least range in line shape with the majority of lines being Gaussian, these lines were also fitted with single Gaussian components for comparison with the parabolic fits. The results for the line velocity from both the parabolic and Gaussian fits are also listed in Table 7.

3. Velocity Structure

Since multiply peaked line profiles and line shoulders can be due to the presence of multiple, unrelated velocity components along the line of sight, rather than the self absorption expected in the presence of infall, it is important to identify the systemic velocity of the gas in which the sources are forming. For this purpose an optically thin spectral line is needed as the line peak velocity of such a line will reflect the mass-weighted average velocity along the line of sight. In this study we have two species which can serve this purpose: N_2H^+ and H^{13}CO^+ .

For the N_2H^+ emission the intensity ratio of the hyperfine components of the transition provide a direct measure of the line optical depth. The optical depth derived from the hyperfine fits (Table 5) show that for the majority of sources the line has an optical depth of less than 1. Although there are some sources with larger values, even for these sources it is unlikely that optical depth significantly affects the estimate of the systemic velocity as the optical depth at the line peak is at very most 0.4 of this total value for broad lines and as little as 0.25 for narrow lines. Although it is harder to estimate the H^{13}CO^+ optical depth, the weakness of the line compared to the HCO^+ 1-0 emission and its simple Gaussian line profile, consistent in width with the N_2H^+ (§ 3.1), suggest the emission is optically thin.

3.1. Systemic Velocities

Since we have observations of two tracers which different authors have used to define source systemic velocities in searches for infall (Mardones et al. , 1997; Gregersen & Evans , 2000), we can compare the properties of these two lines to determine whether these species are tracing the same material. One test is to compare the linewidth of the H^{13}CO^+ and that derived from the hyperfine fit to the N_2H^+ . Figure 3 shows the N_2H^+ linewidths and the ratio of the H^{13}CO^+ linewidth to the N_2H^+ linewidth. The mean linewidth ratio is 1.11 ± 0.03 (the quoted uncertainty is the standard error on the mean). Although this result suggests

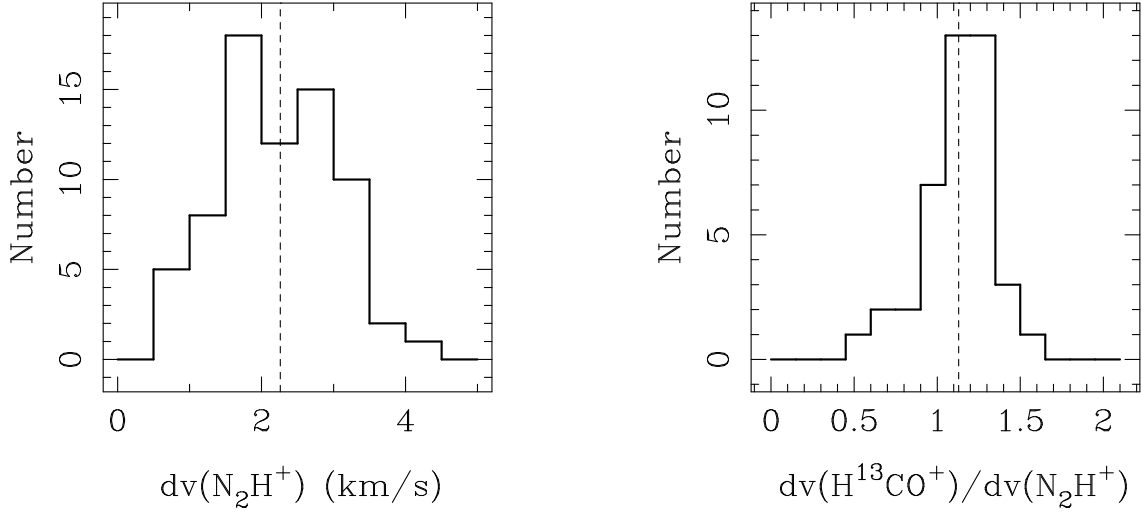


Fig. 3. The left panel shows the distribution of N_2H^+ linewidths of the sources. The vertical dashed line indicates the median N_2H^+ linewidth of 2.26 km s^{-1} . The right panel shows the ratio of $H^{13}CO^+$ linewidth to N_2H^+ linewidth. The median value of 1.13 indicated by the dashed vertical line.

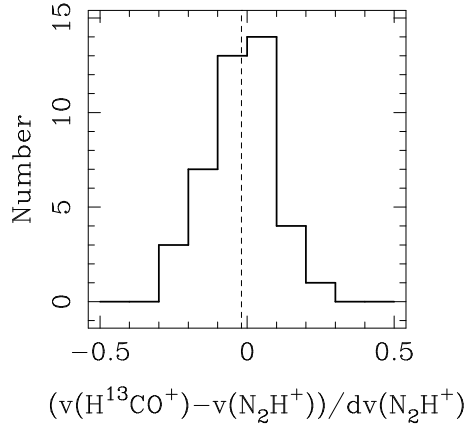


Fig. 4. Comparison of N_2H^+ and $H^{13}CO^+$ velocities. The figure shows the difference in velocity between $H^{13}CO^+$ and N_2H^+ in units of the N_2H^+ linewidth. The vertical dashed line marks the median value of -0.02 . All the sources for which the $H^{13}CO^+$ was detected with a line peak temperature greater than 2.5 times the rms noise level in the spectrum are included in the figure.

that on average the linewidth of the $H^{13}CO^+$ is $\sim 10\%$ larger than that of the N_2H^+ , this relatively small difference suggests that these two species trace very similar material. Figure 4 shows the difference in line velocity in units of the N_2H^+ line width. The mean value of this quantity of -0.03 , with a standard error on the mean of 0.02 , again showing that in general these lines are tracing the same material associated with the forming stars.

Since these tracers appear to be tracing the same material around the sources, but our observations of N_2H^+ have higher signal to noise and we detect it towards a larger fraction of the sources, we choose to adopt the N_2H^+ velocity as the source systemic velocity.

4. Line Asymmetries

To quantify the blue asymmetry of a line we use the Mardones et al. (1997) asymmetry parameter, δv , which is defined as the difference between the line peak velocity of an optically thick tracer, $v(\text{thick})$, and an optically thin tracer, $v(\text{thin})$, measuring the systemic velocity, in units of the optically thin line width, $dv(\text{thin})$,

$$\delta v = \frac{v(\text{thick}) - v(\text{thin})}{dv(\text{thin})} \quad (1)$$

where we use N_2H^+ as the optically thin tracer.

Table 7 and Figure 5 summarize the asymmetry parameter measurements for the $HCO^+ \text{ J} = 1 \rightarrow 0$, $\text{J} = 3 \rightarrow 2$, $\text{J} = 4 \rightarrow 3$ and H_2CO spectra, measured with respect to the N_2H^+ velocity and line width. Negative values correspond to blueshifted emission

Table 5. Hyperfine fits to N_2H^+ spectra. For each source the table gives (in order) the velocity of the emission, the FWHM velocity width of the emission, the line optical depth, the line peak temperature in units of T_A^* , derived from the fit to the hyperfine structure, and the rms in an emission-free region of the spectrum and the rms residual in the region of the line after fitting to the hyperfine structure of the line. The values in parenthesis are the one standard deviation uncertainties in the associated quantities. The quoted optical depth is the peak optical depth the emission would have in the absence of the hyperfine structure.

Source	V	dv	τ	T_{peak}	Baseline rms	Line rms	Source	V	dv	Tau	T_{peak}	Baseline rms	Line rms
	(km/s)	(km/s)		(K)	(K)	(K)		(km/s)	(km/s)		(K)	(K)	(K)
2	-16.10 (0.01)	2.71 (0.01)	0.11 (0.01)	7.03	0.07	0.26	55	49.65 (0.01)	3.17 (0.02)	0.10 (0.02)	2.26	0.07	0.08
5	0.72 (0.03)	1.00 (0.08)	1.09 (1.25)	0.48	0.07	0.07	59	77.18 (0.02)	2.54 (0.04)	0.11 (0.01)	1.56	0.07	0.10
3	0.22 (0.01)	1.43 (0.05)	0.47 (0.38)	1.26	0.07	0.08	62	49.52 (0.12)	1.65 (0.28)	0.10 (0.94)	0.14	0.06	0.05
6	6.03 (0.09)	1.61 (0.21)	0.10 (0.95)	0.21	0.07	0.07	64	10.83 (0.02)	3.14 (0.05)	0.42 (0.19)	0.93	0.04	0.05
8	32.56 (0.01)	3.36 (0.01)	0.77 (0.06)	3.13	0.07	0.21	65	85.12 (0.01)	3.04 (0.03)	1.80 (0.14)	2.29	0.08	0.12
12	111.03 (0.03)	2.92 (0.08)	0.35 (0.31)	0.95	0.06	0.09	66	66.04 (0.02)	2.53 (0.05)	1.26 (0.24)	0.78	0.04	0.04
13	21.88 (0.01)	3.53 (0.01)	3.41 (0.02)	3.01	0.06	0.24	67	32.83 (0.02)	4.13 (0.04)	0.30 (0.12)	1.64	0.06	0.07
14	33.23 (0.01)	1.88 (0.02)	0.90 (0.13)	0.69	0.02	0.02	68	55.11 (0.01)	2.80 (0.01)	0.10 (0.01)	1.08	0.06	0.06
15	59.96 (0.01)	2.48 (0.01)	0.10 (0.01)	2.44	0.06	0.08	70	7.05 (0.07)	2.08 (0.18)	0.10 (0.51)	0.32	0.07	0.07
16	59.76 (0.01)	3.09 (0.01)	0.11 (0.01)	4.00	0.06	0.15	71	14.05 (0.04)	2.29 (0.13)	2.44 (0.78)	0.45	0.06	0.08
17	45.12 (0.01)	1.86 (0.01)	1.11 (0.07)	3.73	0.06	0.13	72	3.11 (0.01)	3.93 (0.02)	0.10 (0.04)	1.94	0.06	0.08
18	120.93 (0.01)	2.87 (0.02)	0.10 (0.02)	1.91	0.06	0.09	73	69.89 (0.03)	3.09 (0.04)	0.73 (0.01)	1.21	0.10	0.10
19	43.73 (0.01)	2.81 (0.01)	0.22 (0.01)	5.33	0.06	0.12	74	5.05 (0.01)	2.93 (0.03)	0.10 (0.05)	2.04	0.09	0.09
20	34.85 (0.06)	1.57 (0.16)	0.10 (0.17)	0.28	0.06	0.07	75	22.95 (0.01)	1.20 (0.02)	2.83 (0.20)	2.47	0.06	0.10
21	34.14 (0.03)	1.10 (0.11)	1.03 (1.18)	0.65	0.08	0.08	79	22.52 (0.01)	1.80 (0.01)	0.91 (0.03)	6.78	0.04	0.18
22	84.56 (0.01)	2.45 (0.04)	1.54 (0.20)	2.91	0.12	0.15	80	29.42 (0.01)	1.74 (0.03)	0.55 (0.22)	1.50	0.06	0.07
23	84.25 (0.01)	2.14 (0.03)	0.68 (0.16)	2.84	0.08	0.13	82	20.42 (0.02)	1.55 (0.06)	4.14 (0.76)	0.61	0.04	0.06
25	77.96 (0.01)	2.59 (0.01)	0.10 (0.01)	4.71	0.09	0.21	85	11.21 (0.03)	1.74 (0.12)	0.34 (0.60)	0.49	0.05	0.06
27	76.74 (0.01)	2.78 (0.03)	0.26 (0.10)	3.99	0.09	0.21	87	5.55 (0.01)	0.82 (0.02)	1.84 (0.52)	1.11	0.05	0.06
28	84.29 (0.01)	2.26 (0.03)	1.88 (0.17)	2.67	0.08	0.18	88	5.85 (0.01)	0.64 (0.02)	2.36 (0.84)	0.82	0.05	0.05
29	58.89 (0.02)	2.57 (0.04)	1.96 (0.25)	1.58	0.08	0.14	90	-3.73 (0.01)	2.02 (0.01)	0.10 (0.01)	5.06	0.05	0.12
30	95.51 (0.01)	3.14 (0.03)	0.80 (0.09)	2.67	0.07	0.15	91	-2.04 (0.01)	0.95 (0.03)	2.20 (0.74)	0.62	0.05	0.05
33	109.70 (0.01)	2.70 (0.01)	0.10 (0.01)	2.83	0.07	0.10	93	-1.65 (0.01)	1.40 (0.03)	0.72 (0.24)	1.52	0.06	0.05
34	22.59 (0.03)	2.75 (0.09)	0.59 (0.39)	0.95	0.08	0.08	94	6.07 (0.01)	1.98 (0.01)	0.36 (0.01)	5.28	0.05	0.14
35	25.52 (0.09)	3.46 (0.22)	0.80 (0.74)	0.42	0.09	0.07	95	8.40 (0.01)	1.35 (0.04)	0.10 (0.07)	0.82	0.05	0.06
36	15.84 (0.05)	1.83 (0.16)	2.37 (1.10)	0.48	0.09	0.08	96	-2.99 (0.02)	1.84 (0.06)	0.59 (0.35)	1.22	0.07	0.08
37	105.17 (0.02)	1.94 (0.07)	1.94 (0.50)	1.14	0.09	0.09	97	-2.14 (0.04)	2.83 (0.08)	0.10 (0.09)	0.80	0.08	0.08
39	96.43 (0.01)	2.33 (0.03)	0.70 (0.12)	1.72	0.04	0.09	100	11.38 (0.01)	2.36 (0.02)	1.58 (0.12)	2.34	0.06	0.11
38	111.55 (0.02)	1.40 (0.07)	6.30 (1.12)	0.92	0.09	0.13	99	10.91 (0.01)	1.43 (0.02)	1.87 (0.14)	2.62	0.06	0.08
42	97.61 (0.01)	2.32 (0.03)	0.10 (0.01)	1.77	0.07	0.09	101	-18.44 (0.01)	1.56 (0.04)	0.12 (0.01)	1.44	0.08	0.08
43	86.86 (0.11)	2.07 (0.34)	0.10 (0.20)	0.21	0.07	0.08	106	-47.96 (0.01)	1.92 (0.05)	0.22 (0.26)	1.45	0.07	0.09
44	102.60 (0.01)	1.72 (0.03)	0.10 (0.01)	2.16	0.07	0.12	107	-45.70 (0.03)	1.57 (0.08)	1.04 (0.59)	0.79	0.07	0.08
48	96.51 (0.02)	3.00 (0.07)	0.14 (0.29)	0.85	0.06	0.07	108	-53.08 (0.01)	2.61 (0.03)	0.38 (0.10)	3.23	0.08	0.09
50	38.96 (0.01)	2.03 (0.01)	0.10 (0.01)	2.24	0.06	0.08	109	-44.41 (0.01)	2.40 (0.04)	0.45 (0.17)	1.93	0.08	0.09
51	83.18 (0.01)	1.68 (0.04)	1.54 (0.32)	1.41	0.07	0.09	110	-54.45 (0.20)	3.26 (0.47)	0.10 (0.22)	0.10	0.05	0.05
54	95.91 (0.04)	2.56 (0.10)	0.10 (0.08)	0.78	0.09	0.09	111	-17.54 (0.03)	1.22 (0.08)	0.84 (0.82)	0.61	0.07	0.07
55	49.65 (0.01)	3.17 (0.02)	0.10 (0.02)	2.26	0.07	0.08	112	-18.83 (0.09)	0.92 (0.25)	0.10 (19.42)	0.16	0.07	0.08
59	77.18 (0.02)	2.54 (0.04)	0.11 (0.01)	1.56	0.07	0.10							

Table 6. Results from Gaussian fits to H^{13}CO^+ spectra. For each source the table gives (in order) the velocity of the emission, the velocity width of the line, the integrated intensity $\int T_A^* dv$, the line peak temperature in units of T_A^* from the fit, the rms in an emission-free region of the spectrum and the rms residual in the region of the line after fitting the Gaussian. The values in parenthesis are the one standard deviation uncertainties in the associated quantities.

Source	V	dv	Int. I.	T	Baseline rms	Line rms	Source	V	dv	Int. I.	T	Baseline rms	Line rms
	(km/s)	(km/s)	(K km/s)	(K)	(K)	(K)		(km/s)	(km/s)	(K km/s)	(K)	(K)	(K)
2	-16.09 (0.03)	2.46 (0.08)	2.74 (0.08)	1.05	0.11	0.12	71	14.06 (0.11)	2.44 (0.27)	0.37 (0.03)	0.14	0.05	0.03
3	0.13 (0.08)	1.38 (0.19)	0.55 (0.06)	0.37	0.12	0.12	72	2.75 (0.09)	5.16 (0.21)	2.53 (0.09)	0.46	0.08	0.07
6	5.67 (0.05)	1.60 (0.11)	0.97 (0.06)	0.57	0.11	0.10	75	22.75 (0.04)	1.75 (0.11)	1.47 (0.08)	0.79	0.12	0.11
8	32.96 (0.03)	4.05 (0.07)	4.91 (0.07)	1.14	0.08	0.15	79	22.23 (0.03)	2.24 (0.09)	2.79 (0.09)	1.17	0.13	0.11
13	21.79 (0.09)	3.73 (0.20)	1.58 (0.07)	0.40	0.08	0.08	80	29.16 (0.09)	1.96 (0.19)	0.83 (0.08)	0.40	0.13	0.11
14	33.27 (0.02)	2.13 (0.04)	3.70 (0.05)	1.63	0.08	0.09	82	19.99 (0.11)	1.72 (0.24)	0.46 (0.06)	0.25	0.05	0.04
16	59.47 (0.05)	3.73 (0.10)	3.34 (0.08)	0.84	0.09	0.12	85	11.08 (0.10)	2.11 (0.23)	0.62 (0.06)	0.28	0.09	0.07
17	45.15 (0.04)	2.46 (0.10)	1.81 (0.06)	0.69	0.08	0.09	88	5.84 (0.03)	0.70 (0.06)	0.29 (0.02)	0.39	0.06	0.06
18	120.71 (0.10)	3.03 (0.24)	2.02 (0.14)	0.63	0.18	0.19	87	5.54 (0.03)	0.90 (0.07)	0.32 (0.02)	0.33	0.06	0.05
19	43.82 (0.02)	3.16 (0.06)	9.33 (0.14)	2.77	0.16	0.20	90	-3.46 (0.02)	3.09 (0.06)	4.80 (0.07)	1.46	0.09	0.09
21	34.38 (0.07)	0.76 (0.29)	0.20 (0.04)	0.25	0.07	0.05	91	-2.03 (0.03)	1.14 (0.08)	0.74 (0.04)	0.61	0.09	0.11
23	84.03 (0.09)	2.73 (0.19)	0.71 (0.04)	0.24	0.06	0.06	93	-1.74 (0.04)	1.39 (0.08)	1.17 (0.06)	0.79	0.12	0.10
25	78.01 (0.11)	2.39 (0.30)	0.84 (0.08)	0.33	0.11	0.11	94	6.05 (0.05)	2.11 (0.11)	1.36 (0.06)	0.60	0.09	0.10
28	83.73 (0.12)	2.14 (0.31)	0.67 (0.08)	0.30	0.12	0.13	95	8.32 (0.06)	1.68 (0.17)	0.69 (0.06)	0.39	0.09	0.08
30	95.52 (0.11)	2.33 (0.27)	1.00 (0.09)	0.40	0.13	0.11	99	10.94 (0.03)	1.66 (0.07)	1.94 (0.07)	1.09	0.12	0.11
35	25.86 (0.17)	4.88 (0.42)	1.59 (0.12)	0.31	0.12	0.11	100	11.40 (0.05)	2.66 (0.10)	2.40 (0.09)	0.85	0.12	0.10
48	96.38 (0.10)	1.73 (0.26)	0.74 (0.09)	0.40	0.14	0.13	101	-18.38 (0.05)	1.39 (0.12)	0.91 (0.07)	0.62	0.12	0.11
65	85.55 (0.15)	3.72 (0.36)	1.99 (0.16)	0.50	0.18	0.19	108	-53.52 (0.11)	3.00 (0.27)	1.18 (0.09)	0.37	0.11	0.09
66	65.69 (0.06)	3.21 (0.15)	1.60 (0.06)	0.47	0.07	0.08	109	-44.13 (0.07)	2.95 (0.17)	2.05 (0.10)	0.65	0.13	0.12
67	33.07 (0.11)	3.90 (0.27)	1.46 (0.09)	0.35	0.10	0.09	111	-17.68 (0.06)	1.58 (0.20)	0.85 (0.08)	0.50	0.12	0.12
68	54.90 (0.09)	2.40 (0.17)	0.72 (0.05)	0.28	0.07	0.09	112	-18.76 (0.06)	1.26 (0.16)	0.62 (0.06)	0.46	0.12	0.13
71	14.06 (0.11)	2.44 (0.27)	0.37 (0.03)	0.14	0.05	0.03							

while positive values are redshifted. For comparison, Table 7 also includes the N_2H^+ and H^{13}CO^+ line velocities as measured by hyperfine fitting and Gaussian fitting respectively, together with the velocity of the HCO^+ $J=4 \rightarrow 3$ transition also derived from a Gaussian fit to the line. Comparing the results from the Gaussian and parabolic fits shows that for the lines which are most Gaussian in shape the two methods produce very good agreement in the fitted velocity. Examination of those eight sources where the results from the two methods differ by more than 0.3 km s^{-1} shows that the line profiles are clearly double peaked or skewed. The rms difference in velocities over all the sources is 0.26 km s^{-1} with a mean difference of 0.03 km s^{-1} , while if only those 65 sources with a velocity difference of less than 0.5 km s^{-1} are considered the rms velocity difference drops to 0.14 km s^{-1} with a mean velocity difference of -0.02 km s^{-1} . This good correspondence between the Gaussian and peak fitted velocities, especially for sources with nearly Gaussian lines confirms that the peak fitting method produces reliable estimates of the line peak velocity.

Most mechanisms producing asymmetric line profiles towards sources, e.g. rotation, should produce approximately equal numbers of red and blue asymmetric profiles, there being no mechanism to favour one colour of asymmetry over the other. On the other hand infall should preferentially produce blue asymmetric profiles (e.g. Anglada et al. 1987; Zhou 1992; Walker, Narayanan & Boss 1994). To quantify whether line profiles of a particular colour dominate in a sample, Mardones et al. (1997) defined a quantity E , the blue excess,

$$E = \frac{N_{\text{blue}} - N_{\text{red}}}{N_{\text{total}}} \quad (2)$$

where N_{blue} and N_{red} are the number of sources which show blue or red asymmetric lines, respectively, and N_{total} is the total number of sources observed. The presence of large blue excesses towards samples of low mass protostars has provided considerable support to the case for the detection of infall around such sources (Mardones et al. , 1997).

To apply the blue excess statistic requires the definition of a range of δv to identify asymmetric sources. Mardones et al. adopted a criterion of $|\delta v| > 0.25$ to indicate that a line profile was asymmetric and for consistency with their analysis we adopt the same criterion. It is important to note however that since the N_2H^+ lines towards this sample of sources is significantly broader than towards low mass sources, the choice of this same bound on δv actually corresponds to a larger absolute velocity shift for these high mass objects than for the lower mass sources. Combining the estimated uncertainties on the measured line velocities and widths we estimate a typical uncertainty in our measured values of δv of 0.02 to 0.05.

The results of measuring the blue excess for the four transitions which are assumed to be optically thick are listed in Table 8. This table shows that for the whole sample of sources observed in HCO^+ $J=3 \rightarrow 2$ and $J=4 \rightarrow 3$ have an equal number of blue and red asymmetric lines. However in both the $J=1 \rightarrow 0$ transition of HCO^+ and H_2CO , there are considerably more blue asymmetric lines than red asymmetric ones, with blue excesses of 15% and 19% for the HCO^+ and H_2CO respectively. In terms of the actual number of sources with significant asymmetries for HCO^+ $J=1 \rightarrow 0$ there are nearly twice as many blue sources as red sources while for H_2CO there are over three times as many blue lines as red ones.

It is of course possible that for any set of observations an excess of blue sources could arise by chance even if the underlying distribution of sources has equal number of red and blue asymmetric line profiles. So in order to assess the statistical significance of the measured blue excesses we have used an exact probability binomial test (Conover, 1971). Given that we have a number of sources which have a significant red asymmetry ($\delta v > 0.25$) or blue asymmetry ($\delta v < -0.25$), if the sources are randomly distributed between red and blue asymmetric, we can calculate the probability that we would observe by chance a blue excess as large as actually measured. We do this by calculating the number of ways it is possible to distribute a number of objects equal to the total of blue plus red asymmetric profiles into two bins, blue and red, and ask how many of these combinations have a number of sources in the blue bin equal to or larger than observed. The ratio of this to the total number of possible combinations is then the probability that the observed excess arises by chance. This probability is listed in Table 8 as the quantity P . A small value of P indicates that it is unlikely that a blue excess as large as observed could arise by chance from an intrinsically uniform distribution.

Table 8 shows that for HCO^+ $J=1 \rightarrow 0$ the excess of blue asymmetric sources as compared to red, the binomial test indicates only a 6% probability of this asymmetry arising by chance. For the H_2CO with a total number of asymmetric sources is 22, 17 blue and 5 red, the probability is just 0.8% that this excess arises by chance. It appears that for these two transitions, but particularly the H_2CO , the excess of blue asymmetric lines is statistically significant.

One point to recall about the sources in this sample is that they span a range of distances from 0.7 to 10.6 kpc (Sridharan et al. , 2002) and for some objects there is an ambiguity between the source near and far kinematic distances leading to the possibility that some sources are at distances as great as 13.6 kpc (Sridharan et al. , 2002). To limit the possibility of including sources at very large distances where the telescope beam may contain emission from material not intimately associated with the high mass protostars, we formed a subsample of objects which have confirmed distances of less than 8kpc and have looked at the blue excess for these objects alone. The median distance of the sources in this subsample is 3.3 kpc.

For this distance limited subsample the blue excess seen in HCO^+ $J=1 \rightarrow 0$ and H_2CO become even more pronounced with blue excess of 28% and 23% respectively and probabilities of only 2% and 3% that these arise by chance. Restricting the sample even further to include only sources with known distances of less than 6 kpc, giving a mean distance of a source of 2.7kpc, the blue excesses become even more significant (Table 8). In the HCO^+ $J=1 \rightarrow 0$ the sample falls to 25 sources, 9 blue and 1 red, giving a blue excess of 0.31 and a mean asymmetry of -0.22 ± 0.09 while for the H_2CO the sample falls to 21 sources, 6 blue

Table 7. Line velocities and asymmetries. Columns 2, 3 and 4 give the line velocities determined from the hyperfine fit to the N_2H^+ and Gaussian fits to the H^{13}CO^+ and HCO^+ $J=4 \rightarrow 3$ respectively. The next four columns give the velocities derived from parabolic fits to the lines and the final four columns the line asymmetry parameter derived from these velocities.

Source	$v(\text{N}_2\text{H}^+)$	$v(\text{H}^{13}\text{CO}^+)$	$v(\text{HCO}^+ 4-3)$	Velocity				δv			
				$\text{HCO}^+(1-0)$	$\text{HCO}^+(3-2)$	$\text{HCO}^+(4-3)$	H_2CO	$\text{HCO}^+(1-0)$	$\text{HCO}^+(3-2)$	$\text{HCO}^+(4-3)$	H_2CO
2	-16.10	-16.09	-14.98	-15.49	...	-14.85	...	0.23	...	0.46	...
3	0.22	0.13	0.27	0.12	...	0.32	...	-0.07	...	0.07	...
5	0.72	0.19	-0.53
6	6.03	5.67	5.83	6.19	...	5.83	...	0.10	...	-0.12	...
8	32.56	32.96	31.57	35.29	31.26	31.59	34.84	0.81	-0.39	-0.29	0.68
12	111.03	...	110.86	111.72	...	110.38	111.60	0.23	...	-0.22	0.20
13	21.88	21.79	21.96	24.80	...	23.42	22.99	0.83	...	0.44	0.31
14	33.23	33.27	33.24	33.26	...	33.21	33.25	0.02	...	-0.01	0.01
15	59.96	...	59.71	60.80	...	59.79	60.49	0.34	...	-0.07	0.22
16	59.76	59.47	58.77	58.41	...	58.88	58.66	-0.44	...	-0.29	-0.36
17	45.12	45.15	45.41	44.54	...	45.19	44.95	-0.31	...	0.04	-0.09
18	120.93	120.71	120.66	120.49	...	120.66	120.54	-0.15	...	-0.10	-0.14
19	43.73	43.82	44.35	44.01	...	44.87	43.79	0.10	...	0.40	0.02
21	34.14	34.38	34.04	32.78	...	34.17	33.96	-1.23	...	0.03	-0.16
20	34.85	...	34.73	32.95	...	34.78	33.95	-1.20	...	-0.04	-0.57
22	84.56	...	83.75	84.76	83.74	83.63	84.17	0.08	-0.34	-0.38	-0.16
23	84.25	84.03	84.17	84.67	...	84.19	84.20	0.20	...	-0.03	-0.02
25	77.96	...	77.98	77.68	...	77.87	77.76	-0.11	...	-0.03	-0.08
27	76.74	...	76.78	77.45	...	77.48	76.98	0.26	...	0.27	0.09
28	84.29	...	84.13	82.79	...	84.89	83.65	-0.66	...	0.27	-0.29
29	58.89	...	59.27	57.56	...	58.87	58.82	-0.52	...	-0.01	-0.03
30	95.51	95.52	96.12	97.30	...	96.28	95.73	0.57	...	0.25	0.07
33	109.70	...	110.35	110.48	...	110.46	110.49	0.29	...	0.28	0.29
34	22.59	...	22.95	20.97	...	22.93	22.31	-0.59	...	0.12	-0.10
35	25.52	...	25.98	27.56	...	25.97	25.25	0.59	...	0.13	-0.08
36	15.84	...	15.81	16.10	...	15.85	15.10	0.14	...	0.00	-0.41
37	105.17	...	105.39	105.60	...	105.36	105.14	0.22	...	0.10	-0.02
39	96.43	...	95.59	95.50	...	95.68	95.53	-0.40	...	-0.32	-0.39
38	111.55	...	111.47	111.53	...	111.45	111.30	-0.02	...	-0.07	-0.18
42	97.61	...	97.97	97.56	...	97.99	97.63	-0.02	...	0.16	0.01
44	102.60	...	102.65	102.65	...	102.66	102.34	0.03	...	0.04	-0.15
48	96.51	...	97.07
50	38.96	...	38.98	38.65	38.75	38.94	38.69	-0.15	-0.10	-0.01	-0.13
51	83.18	...	83.17	82.10	...	83.15	82.68	-0.64	...	-0.01	-0.30
55	49.65	...	49.51	47.86	...	49.56	48.56	-0.57	...	-0.03	-0.34
59	77.18	...	77.22	74.92	76.08	76.84	76.15	-0.89	-0.43	-0.13	-0.41

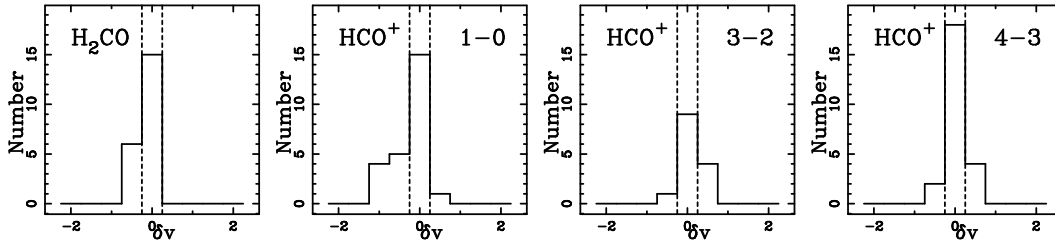
Table 7 continued.

Source	v(N ₂ H ⁺)	v(H ¹³ CO ⁺)	v(HCO ⁺ 4-3)	Velocity				δv			
				HCO ⁺ (1-0)	HCO ⁺ (3-2)	HCO ⁺ (4-3)	H ₂ CO	HCO ⁺ (1-0)	HCO ⁺ (3-2)	HCO ⁺ (4-3)	H ₂ CO
62	49.52	...	49.70	50.20	...	49.70	49.91	0.41	...	0.11	0.24
64	10.83	...	10.15	9.04	9.84	10.11	9.70	-0.57	-0.32	-0.23	-0.36
65	85.12	...	87.45	88.00	87.58	87.40	87.00	0.95	0.81	0.75	0.62
66	66.04	65.69	65.51	65.97	64.38	65.11	64.93	-0.03	-0.65	-0.37	-0.44
67	32.83	33.07	32.94	32.38	32.41	32.68	32.71	-0.11	-0.10	-0.04	-0.03
68	55.11	54.90	54.94	54.81	55.15	54.94	54.91	-0.11	0.01	-0.06	-0.07
71	14.05	14.06	14.38	14.58	...	14.31	14.47	0.23	...	0.12	0.18
70	7.05	...	6.45	6.99	7.17	6.40	6.94	-0.03	0.06	-0.32	-0.05
72	3.11	2.75	3.43	3.45	...	3.48	3.18	0.09	...	0.09	0.02
73	69.89	...	69.14	68.65	68.59	69.04	68.72	-0.40	-0.42	-0.28	-0.38
74	5.05	5.10	5.14	0.02	0.03
75	22.95	22.75	22.89	22.74	...	22.88	22.90	-0.18	...	-0.06	-0.04
79	22.52	22.23	21.85	21.38	...	21.72	22.06	-0.64	...	-0.44	-0.26
80	29.42	29.16	29.76	29.43	...	29.90	29.49	0.00	...	0.27	0.04
82	20.42	19.99	20.04	19.69	...	19.74	19.77	-0.48	...	-0.44	-0.42
85	11.21	11.08	11.03	12.49	...	11.11	12.13	0.73	...	-0.06	0.53
88	5.85	5.84	5.63	5.44	...	5.61	5.65	-0.65	...	-0.37	-0.32
87	5.55	5.54	5.51	4.79	...	5.50	5.52	-0.93	...	-0.06	-0.04
90	-3.73	-3.46	-3.18	-3.27	...	-2.94	-3.55	0.23	...	0.39	0.09
91	-2.04	-2.03	-1.79	-2.20	...	-1.79	-1.83	-0.17	...	0.26	0.21
93	-1.65	-1.74	-1.45	-1.60	-1.46	-1.54	-1.63	0.03	0.13	0.07	0.01
94	6.07	6.05	6.28	6.24	6.52	6.23	6.29	0.09	0.23	0.08	0.11
95	8.40	8.32	8.55	8.59	8.68	8.58	8.49	0.14	0.21	0.14	0.07
96	-2.99	...	-2.66	-3.75	-2.77	-2.68	-3.55	-0.41	0.12	0.17	-0.30
97	-2.14	...	-1.66	-2.67	-1.31	-1.62	-1.69	-0.19	0.29	0.18	0.16
99	10.91	10.94	10.92	11.12	10.73	10.96	11.16	0.15	-0.12	0.03	0.17
100	11.38	11.40	11.34	11.41	11.22	11.32	11.48	0.01	-0.07	-0.03	0.04
101	-18.44	-18.38	-18.20	-17.40	-17.50	-18.18	-18.84	0.66	0.60	0.16	-0.26
106	-47.96	...	-47.99	-48.13	-47.71	-47.93	-47.74	-0.09	0.13	0.01	0.11
107	-45.70	...	-45.54	-45.55	-45.60	-45.53	-45.74	0.10	0.06	0.11	-0.02
108	-53.08	-53.52	-52.83	-53.27	-52.48	-52.58	-53.05	-0.07	0.23	0.19	0.01
109	-44.41	-44.13	-43.32	-45.07	-43.08	-43.10	-44.67	-0.27	0.56	0.55	-0.11
111	-17.54	-17.68	-17.65	-18.65	-17.16	-17.70	-17.86	-0.91	0.31	-0.13	-0.27

Table 8. Blue excess statistics. The table shows for each transition the number of sources with blue asymmetric lines, red asymmetric lines and the total number of sources, the blue excess, E , the probability, P , of such an excess and the mean asymmetry and the standard error on the mean.

Transition	N_{blue}	N_{red}	N_{total}	E	P	Mean $\delta v \pm \text{sem}$
HCO ⁺ J= 1 → 0	21	11	68	0.15	0.06	-0.08 ± 0.05
HCO ⁺ J= 3 → 2	6	5	24	0.04	0.50	0.03 ± 0.07
HCO ⁺ J= 4 → 3	10	11	66	-0.02	0.67	0.03 ± 0.03
H ₂ CO	17	5	64	0.19	0.008	-0.05 ± 0.03
Distance < 6kpc subsample						
HCO ⁺ J= 1 → 0	9	1	25	0.32	0.01	-0.22 ± 0.09
HCO ⁺ J= 3 → 2	1	4	14	-0.21	0.97	0.14 ± 0.07
HCO ⁺ J= 4 → 3	2	4	24	-0.08	0.89	0.07 ± 0.04
H ₂ CO	6	0	21	0.29	0.02	-0.07 ± 0.04

Fig. 5. Asymmetry for the four transitions for the sample of objects with known distances of <6 kpc. The dashed lines mark the $|\delta v| < 0.25$ region which defines the spectra with no asymmetry.



and none red, giving an excess of 0.32 with a mean asymmetry of -0.07 ± 0.04 . The associated probabilities drop to 1% and 2% respectively.

In comparing the statistical significance of the blue excesses in this survey with other surveys for infall it is important to note that other surveys have not used this exact binomial test which we have used. For example, Mardones et al. (1997) used the Student-t test to compare the distribution of δv with a normal distribution with zero mean. This kind of test makes an assumption about the nature of the underlying distribution of asymmetries, including those sources which do not show any asymmetry. However there are many reasons why a source may not show an infall asymmetry which do not fit well with the hypothesis of smooth distribution of asymmetries assumed by the Student-t test. For example a source might be at a slightly different evolutionary stage, or might not quite have the excitation conditions necessary to produce the asymmetry. We therefore prefer the binomial test which, once stating a criterion which defines which sources have asymmetric profiles, only considers those sources. However, for the sake of comparison applying the Student t-test to just those sources which have a measured asymmetry (which is not how, for example, Mardones et al. (1997) used the test) does produce probabilities similar to but somewhat larger than those given by our binomial test. For example, for the HCO⁺ J= 1 → 0 data on the whole sample, the Student t-test gives a probability of the observed distribution of blue and red sources arising by chance of 0.08, similar to the 0.06 from the binomial test. Applied to the whole sample of asymmetry parameters for the same line in the < 6kpc subsample, the Student t-test gives a probability of 0.025, compared to 0.01 for the binomial test applied to only the asymmetric lines.

As mentioned in Section 2.1, there are a number of sources for which the residuals after fitting the simple single velocity component model for the N₂H⁺ suggest the presence of additional emission. However the presence of these sources in the sample do not significantly distort the measured blue excess. To demonstrate this we have excluded from the sample all the sources for which the rms of the single component fit is greater than 1.6 times the rms in the line free region of the spectra and recalculated the blue excess statistics. For the remaining sources there are 15 blue and 7 red out of 50 HCO⁺ J= 1 → 0 spectra giving a blue excess of 0.16 with an associated probability of 7%, while for the 47 remaining H₂CO spectra, there are 13 blue and 3 red giving a blue excess of 0.21 with a probability of 1%. Comparing these values with those in Table 8 shows that the relatively poorly fitted sources are having negligible effect on the statistics. The same is true if the 6kpc subsample is examined.

For both the 8kpc and 6kpc samples, both HCO⁺ J= 4 → 3 and J= 3 → 2 show relatively large *negative* blue excesses, in other words, an excess of red asymmetric lines. However in no case does the probability show this excess to be less than a 11% probability of being due to chance and so these red excesses appear consistent with chance variations due to sampling.

A comparison of the asymmetry parameter measured towards all the sources observed in both HCO⁺ J= 1 → 0 and H₂CO is shown in Figure 6. The asymmetry of these lines is relatively well correlated, but for majority of the sources the asymmetry of the H₂CO is less than half that of the HCO⁺ perhaps suggesting that these two lines are probing some what different regions around the stars. This would be consistent with the different critical densities of these two transitions, $5 \times 10^4 \text{ cm}^{-3}$ and $2 \times 10^6 \text{ cm}^{-3}$ for

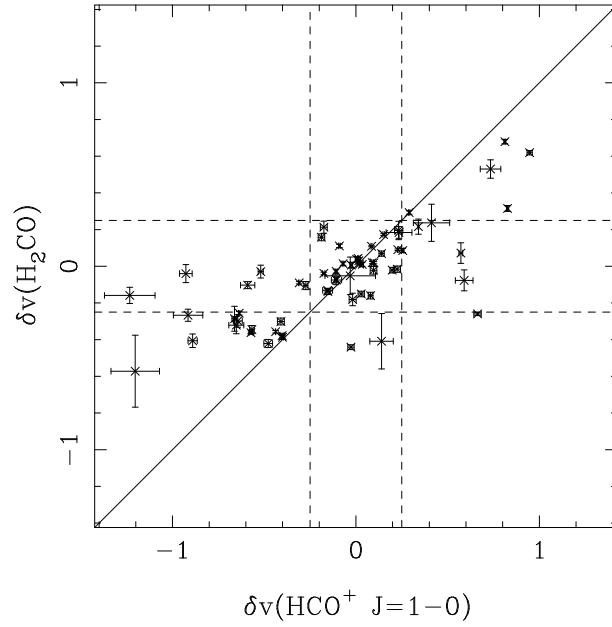


Fig. 6. Comparison of the measured asymmetry in $\text{HCO}^+ J=1 \rightarrow 0$ and H_2CO . The dashed lines mark line of equality is shown in solid.

the HCO^+ and H_2CO respectively. Interestingly the two transitions which show the least blue asymmetry, $\text{HCO}^+ J=3 \rightarrow 2$ and $J=4 \rightarrow 3$, also have the highest critical densities ($3 \times 10^6 \text{ cm}^{-3}$ and $9 \times 10^6 \text{ cm}^{-3}$ respectively) perhaps suggesting stronger infall in the lower density, outer regions of these sources. However until the molecular excitation and line formation in the circumstellar regions of these sources have been modelled in detail, this should only be regarded as speculation.

Table 9. Summary of sources with at least one significant line asymmetry. Entries marked R or B indicate red and blue asymmetric line profile respectively. A dash (–) indicates a line profile with no significant asymmetry and the absence of an entry indicates no observation. Sources marked * are considered the best infall candidates.

Source	HCO^+			H_2CO	Source	HCO^+			H_2CO
	$1 \rightarrow 0$	$3 \rightarrow 2$	$4 \rightarrow 3$			$1 \rightarrow 0$	$3 \rightarrow 2$	$4 \rightarrow 3$	
2	–		R		55 *	B		–	B
5 *	B				59 *	B	B	–	B
8	R	B	B	R	62	R		–	–
13	R		R	R	64 *	B	B	–	B
15	R		–	–	65	R	R	R	R
16 *	B		B	B	66 *	–	B	B	B
17 *	B		–	–	70 *	–	–	B	–
19	–		R	–	73 *	B	B	B	B
21 *	B		–	–	79 *	B		B	B
20 *	B		–	B	80	–		R	–
22 *	–	B	B	–	82 *	B		B	B
27	R		R	–	85	R		–	R
28	B		R	B	87 *	B		–	–
29 *	B		–	–	88 *	B		B	B
30	R		–	–	90	–		R	–
33	R		R	R	91	–		R	–
34 *	B		–	–	96 *	B	–	–	B
35	R		–	–	97	–	R	–	–
36 *	–		–	B	101	R	R	–	B
39 *	B		B	B	109	B	R	R	–
51 *	B		–	B	111	B	R	–	B

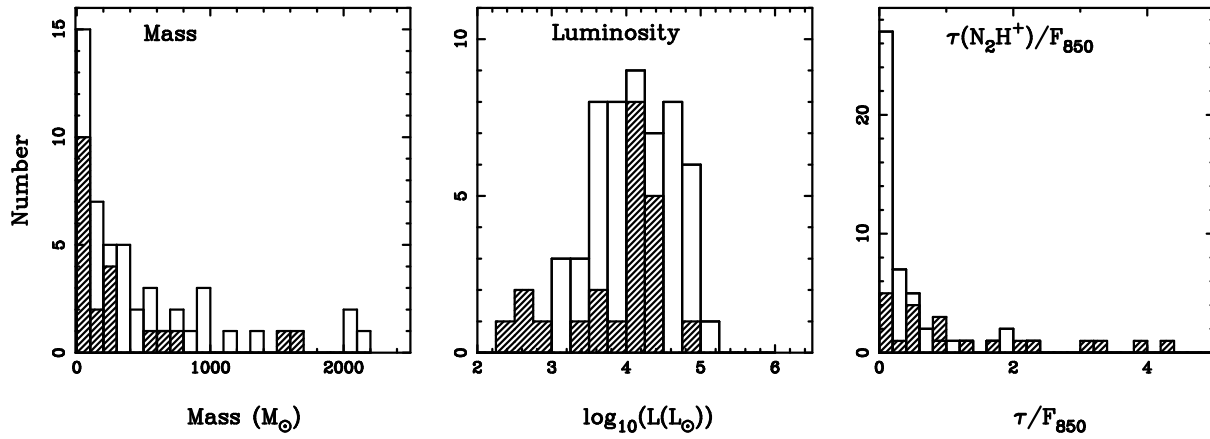


Fig. 7. Comparison of the properties of the infall candidates (shaded) and the other sources in the sample (outline). The left panel shows the distribution of mass derived from the $850\mu\text{m}$ observations of Williams et al. (2004) for the infall candidates and the non-infall sources. The centre panel similarly compares the distribution of the IRAS luminosity, assuming the near kinematic distances for the sources where the distance is ambiguous (Sridharan et al., 2002). The right panel shows the distribution of the ratio of the N_2H^+ optical depth to the $850\mu\text{m}$ flux as discussed in Section 5.

4.1. Comparison with Other Surveys

The level of blue excess seen in this sample of high-mass objects is comparable to that accepted as evidence of infall in similar surveys of low-mass star forming regions. For example, over their whole sample Mardones et al. (1997) find an excess of 0.25, while for several surveys using $\text{HCO}^+ J=3 \rightarrow 2$ transitions, Evans (2003) quotes excesses of 0.30 to 0.31.

In a recent survey of a different sample of young high mass sources using different tracers Wu & Evans (2003) found an excess of 0.21 to 0.29, again very similar to the values found here. Interestingly there is one object in common between this survey and that of Wu & Evans. The source WFS 79 (IRAS 19410+2336) is listed in Wu & Evans as 59.78 ± 0.06 . While they find a velocity for this source of $22.63 \pm 0.07 \text{ km s}^{-1}$ and an optically linewidth of 2.36 km s^{-1} , the N_2H^+ transition is somewhat narrower with a width of 1.8 km s^{-1} and a slightly lower velocity of $22.52 \pm 0.01 \text{ km s}^{-1}$. Nevertheless, both surveys find blue asymmetric line profiles towards this source with all three transitions observed here significantly blue asymmetric.

5. Infall Candidates

The observations of multiple transitions towards the sources in this survey provides a second approach to investigate whether there is infall around the sources. Since infall is expected to preferentially produce blue asymmetric lines, it seems reasonable to expect that this asymmetry should be present in different transitions observed towards the sources. In particular the presence of multiple blue asymmetric transitions and the absence of contradictory information, in the form of red asymmetric profiles, could provide a good criterion for identifying sources with infall, independent of the overall excess of blue line profiles in the sample.

Table 9 summarises those sources which have at least one significantly asymmetric line and from this table we can identify those sources we believe to be the best infall candidates. We do this by requiring an infall candidate to have at least one blue asymmetric transition and no red asymmetric line profiles. This criterion, which is the same as that used by Mardones et al. (1997) produces 22 promising infall candidates. The majority of these candidates, 14 sources, in fact have two or more blue asymmetric profiles and no red profiles.

The 22 infall candidates range in luminosity from $10^{2.4}L_\odot$ up to $10^{4.8}L_\odot$ with a median luminosity of $10^{4.0}L_\odot$ and span a range of distances from 0.6kpc to 10.6kpc but only two sources are at distances greater than 5.5 kpc, assuming near kinematic distances for sources whose distance ambiguity has not been resolved. At these distances the JCMT and IRAM beams are sampling regions 0.02pc to 0.4pc (0.6 to $12 \times 10^{17}\text{cm}$) in radius around the sources. The submillimetre derived mass of the cores around the infall candidates range from several to over a thousand solar masses with a median value of $144M_\odot$.

A comparison of IRAS derived luminosity of the sources (Sridharan et al., 2002) and the mass derived from the $850\mu\text{m}$ observations (Williams et al., 2004) for the infall candidates and the other sources in the sample is shown in Figure 7. Applying a two sample Kolmogorov-Smirnov (K-S) test shows that there is no evidence for a difference in either mass or luminosity between the two groups of objects. Similarly K-S tests show there is no significant difference in the N_2H^+ linewidths, $850\mu\text{m}$ column density, mass to luminosity ratio, $850\mu\text{m}$ to $450\mu\text{m}$ spectral index or cold component dust temperature (Sridharan et al., 2002) between the infall candidates and other sources. Inspection of the radio continuum emission and maser properties (Sridharan et al., 2002) also shows that the infall candidates do not have any different range of properties to the other sources in the sample.

However, the K-S test does indicate that there are differences (at a confidence level of about 98%) between the infall candidates and the remainder of the sample in terms of the optical depth of the N_2H^+ and the $850\mu\text{m}$ peak flux and, at a somewhat

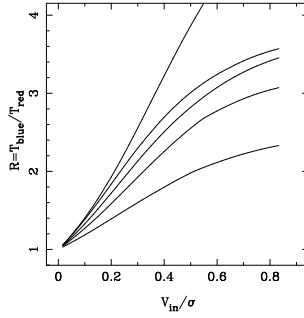


Fig. 8. Line peak intensity ratio $R = T_{\text{blue}}/T_{\text{red}}$ as a function of infall velocity in units of the velocity dispersion, V_{in}/σ . The line profiles were calculated for five different models using the two layer model of Myers et al. (1996).

lower significance level, the $850\mu\text{m}$ integrated flux. The distributions of these quantities suggest that the infall candidates have higher N_2H^+ optical depth and less dust continuum emission than the other sources. Figure 7 shows the distributions of the ratio of the N_2H^+ optical depth to $850\mu\text{m}$ peak flux, which shows a similar difference between the infall and non-infall sources with the infall candidates having a higher ratio of N_2H^+ to dust emission. Although the statistical significance of this difference is not conclusive, if real it has interesting implications about the state of these sources. N_2H^+ is primarily destroyed by reacting with CO (Herbst et al., 1975), leading to high N_2H^+ abundances in regions in which CO is depleted Bergin et al. (2001). Larger CO depletion towards the infall candidates might suggest that these sources are less evolved having not (yet) been as extensively heated by their embedded sources as the non-infall sources. A direct test of this will be to measure the CO depletion towards these sources.

5.1. Infall Properties

If further observations of these candidate sources supports their identification as having infall, then detailed modelling of the temperature, density, velocity and indeed chemical structure of the sources will be needed to derive the properties of the infall. However an order of magnitude estimate of the mass accretion rate can be derived from applying the two layer model of Myers et al. (1996). In an infalling region the strength of the blue-red asymmetry of a line, as measured by R the ratio of the intensity of the blue line peak compared to the red line peak, depends strongly on the infall velocity. Figure 8 shows this intensity ratio as a function of the infall velocity (V_{in}) in units of the velocity dispersion (σ) calculated using the Myers et al. two layer model.

For lines with small asymmetries, $R = T_{\text{blue}}/T_{\text{red}} \lesssim 1.5$, the infall velocity is relatively tightly constrained. For $R = 1.5$ the infall velocity is between ~ 0.1 and ~ 0.25 times the velocity dispersion. For more asymmetric lines the infall velocity exceeds 0.25 times the velocity dispersion and can become comparable to, or greater, than the velocity dispersion. For the sources and transitions in this survey with blue asymmetric lines which show double peak profiles, the value of R is always in excess of 1.2 with values ranging up to 3, implying infall velocities from 0.15 to > 1 times the velocity dispersion. There are also clearly blue asymmetric line profiles for which a red peak can not be identified suggesting even larger infall velocities. Adopting the N_2H^+ linewidth as a measure of the velocity dispersion in the circumstellar material this translates into infall velocities between $\sim 0.1 \text{ km s}^{-1}$ and 1 km s^{-1} with a typical value of $\sim 0.2 \text{ km s}^{-1}$. Adopting a size for the infall region similar to the submillimeter maps of WFS, $9 \times 10^{17} \text{ cm}$ and a number density of $5 \times 10^4 \text{ cm}^{-3}$ this range of infall velocities implies mass infall rates of between $2 \times 10^{-4} M_{\odot}/\text{yr}$ and $10^{-3} M_{\odot}/\text{yr}$.

This range of infall rates is consistent that values inferred from observations of outflows from these sources (Beuther et al., 2002b), although those rates refer to the region where the stellar winds are generated, much closer the central source than the observations presented here. Interestingly the lower end of the range of infall rates is also similar to the rates derived for some low-mass sources. For example, the low luminosity source NGC 1333 IRAS4A has an infall rate of $1.1 \times 10^{-4} M_{\odot}/\text{yr}$ (Di Francesco et al., 2001).

6. Summary

A survey of up to six transitions of HCO^+ , H^{13}CO^+ , H_2CO and N_2H^+ has been carried out towards a sample of 77 submillimetre sources associated with a well selected sample of IRAS sources believed to be high mass protostellar objects.

Emission from N_2H^+ was detected towards all the sources except for a few cases where the observation was significantly offset from the peak of the submillimetre emission. The strength of the N_2H^+ towards the majority of sources and its weakness towards these offset positions suggests that the N_2H^+ and dust continuum emission are tracing similar material. The N_2H^+ is mostly optically thin and typically well modelled by a single Gaussian velocity component. The N_2H^+ velocity and linewidth are

typically in good agreement with those measured for the same source in H^{13}CO^+ , which is also believed to be optically thin and is also well modelled by a single Gaussian component.

Using the N_2H^+ velocity as a measure of the systemic velocity of the circumstellar material associated with the forming stars in these sources, the lines of HCO^+ and H_2CO show a range of profile shapes from near Gaussian, centred at the systemic velocity or offset, to double peaked. Analysis of the asymmetry of the line profiles shows that in HCO^+ $J=1 \rightarrow 0$ and H_2CO there is a statistically significant excess of blue asymmetric line profiles compared to red asymmetric profiles. This excess is larger if the sample is restricted to exclude the most distant sources. Since the emission from infalling material around a central heating source is known to produce systematically blueshifted line profiles, this excess is interpreted as statistical evidence that the material around these sources is infalling, as has been argued for similar samples of nearby low mass protostars.

From the observations of multiple lines, we identify a sample of 22 strong infall candidates none of which show any red asymmetric line profiles and have at least one blue asymmetric profile. Confirmation of the presence of infalling material around these sources requires further observations, in particular maps of the sources to study the spatial distribution of the blue asymmetric profiles and higher angular resolution observations to better probe the inner material close to the central sources, together with detailed modelling of the sources. Nevertheless, the blue asymmetric line profiles together with density and size estimates from submillimetre maps of the sources allow estimates of the range of infall velocity which is found to be between 0.1 km s^{-1} and 1 km s^{-1} and the mass infall rate which is estimated to be between $2 \times 10^{-4} M_{\odot}/\text{yr}$ and $10^{-3} M_{\odot}/\text{yr}$. Even the smallest estimate is consistent with the mass infall rates needed to form a $10 M_{\odot}$ in $\sim 10^5$ years (McKee & Tan, 2002).

Acknowledgements. Part of this work was supported by a PPARC grant to the UMIST Astrophysics Grant and a PPARC studentship to SJW. We would like to thank the staff at both the JCMT and IRAM 30m for their assistance in acquiring the observations presented here.

References

- Andelson, L.M., Leung, C.M. 1988, MNRAS, 235, 349
 Anglada, G., Rodriguez, L.F., Canto, J., Estalella, R., Lopez, R. 1987, AA, 186, 280
 Belloche, A., André, P., Despois, D., Blinder, S. 2002, A&A, 393, 927
 Bergin, E.A., Ciardi, D.R., Lada, C. J., Alves, J, Lada, E.A. 2001, ApJ, 557, 209
 Beuther, H., Schilke, P., Menten, K. M., Motte, F., Sridharan, T. K., Wyrowski, F. 2002, ApJ, 566, 945
 Beuther, H., Schilke, P., Sridharan, T. K., Menten, K. M., Walmsley, C. M., Wyrowski, F. 2002, A&A, 383, 892
 Bonnell, I. A., Bate, M.R., Zinnecker, H. 1998, MNRAS, 298, 93
 Bonnell, I. A., Vine, S.G. Bate, M.R. 2004, MNRAS, 349, 735
 Caselli, P., Myers, P.C., Thaddeus, P. 1995, ApJ, 455, L77
 Conover, W. J. 1971, Practical nonparametric statistics. New York: John Wiley & Sons. Pages 97-104.
 Di Francesco, J., Myers, P.C., Wilner, D.J., Ohashi, N., & Mardones, D. 2001, ApJ, 562, 770
 Evans, N. J., II. 2003, in Chemistry as a Diagnostic of Star Formation, University of Waterloo, Canada, 2002 August 2123, ed. C. L. Curry & M. Fich
 Gregersen, E.M., Evans, N.J., II. 2001, ApJ, 553, 1042
 Gregersen, E.M., Evans N.J, II. 2000, ApJ, 538, 260
 Gregersen, E.M., Evans N.J, II., Mardones, D., Myers, P.C. 2000, ApJ, 533, 440
 Herbst, E., Payzant, J. D., Schiff, H. I., Bohme, D. K. 1975, ApJ, 201, 603
 Lee, C. W., Myers, P.C., Tafalla, M. 1999, ApJ, 526, 788
 Lee, C. W., Myers, P.C., Tafalla, M. 2001, ApJS, 136, 703
 Lee, C. W., Myers, P. C., Plume, R. 2004, ApJS, 153, 523
 Leung, C.M., Brown, R.L. 1977, ApJ, 214, L73
 Lovas, F.J "NIST Recommended Rest Frequencies for Observed Interstellar Molecular Microwave Transitions - 1991 Revision" (version 1.1), [Online]. Available: <http://physics.nist.gov/restfreq> [2003, January 30]. National Institute of Standards and Technology, Gaithersburg, MD.
 Lovas, F.J 1992, J. Phys. Chem. Ref. Data 21, 181
 Lumsden, S. L., Hoare, M. G., Oudmaijer, R. D., & Richards, D. 2002, MNRAS, 336, 621
 Mardones, D., Myers, P.C., Tafalla, M., Wilner, D.J., Bachiller, R., Garay, G. 1997, ApJ, 489, 719
 McKee, C.F., Tan, J.C. 2002, Nature, 416, 59
 McKee, C.F., Tan, J.C. 2003, ApJ, 585, 850
 Molinari, S., Brand, J., Cesaroni, R., & Palla, F. 1996, A&A, 308, 573
 Myers, P.C., Mardones, D., Tafalla, M., Williams, J.P., Wilner, D.J. 1996, ApJ, 465, L133
 Park, Y.-S., Kim, J., Minh, Y. C. 1999, ApJ, 520, 223
 Pickett, H. M., Poynter, R. L., Cohen, E. A., Delitsky, M. L., Pearson, J.C., & Muller, H. S. P. 1998, J. Quant. Spectrosc. & Rad. Transfer 60, 883-890 (<http://spec.jpl.nasa.gov/>)
 Ramesh, B. & Sridharan, T. K. 1997, MNRAS, 284, 1001

- Sridharan, T.K., Beuther, H., Schilke, P., Menten, K.M., Wyrowski, F. 2002, ApJ, 566, 931
Walker, C.K., Narayanan, G., Boss, A.P. 1994, ApJ, 431, 767
Williams, J.P., Myers, P.C., Wilner, D.J., di Francesco, J. 1999, ApJ, 513, L61
Williams, S.J., Fuller, G.A., Sridharan, T.K. 2004, A&A, 417, 115
Williams, S.J., Fuller, G.A., Sridharan, T.K. 2005, A&A, 434, 257
Wood, D.O.S., Churchwell, E. 1989, ApJ, 340, 265
Wu, J., Evans, N.J. 2003, ApJ, 592, L79
Zhou, S. 1992, ApJ, 394, 204